An implantable piezoelectric ultrasound stimulator (ImPULS) for selective deep brain activation

by

Jason F. Hou

B.S., University of California, Berkeley (2019)

Submitted to the Program in Media Arts and Sciences, School of Architecture and Planning, in partial fulfillment of the requirements for the degree of

Master of Science

at the

MASSACHUSETTS INSTITUTE OF TECHNOLOGY

June 2023

AUTHORED BY

Jason F. Hou
Program in Media Arts and Sciences
May 19, 2023

CERTIFIED BY

Dr. Canan Dagdeviren
Associate Professor of Media Arts and Sciences
Thesis Supervisor

ACCEPTED BY

Dr. Tod Machover
Academic Head
Program in Media Arts and Sciences

An implantable piezoelectric ultrasound stimulator (ImPULS) for selective deep brain activation

by

Jason F. Hou

Submitted to the Program in Media Arts and Sciences, School of Architecture and Planning
on May 19, 2023, in partial fulfillment of the
requirements for the degree of
Master of Science

Abstract

Precise neurostimulation has potential to revolutionize therapies for neurological disorders. However, current neural interfaces targeting the deep brain face significant limitations in spatial resolution and potency due to tissue attenuation. We developed an implantable piezoelectric ultrasound stimulator (ImPULS) that generates an ultrasonic focal point pressure of 100 kPa and can non-genetically modulate the activity of neurons. We demonstrated that ImPULS can i) excite neurons in a mouse hippocampal slice ex vivo, ii) activate cells in the hippocampus of an anesthetized mouse to induce expression of activity-dependent gene c-Fos, and iii) stimulate dopaminergic neurons in the substantia nigra pars compacta (SNc) to elicit time-locked modulation of nigrostriatal dopamine release. This work introduces a novel, non-genetic ultrasound platform for spatially localized neural stimulation.

Thesis Supervisor: Canan Dagdeviren
Title: Associate Professor of Media Arts and Sciences

An implantable piezoelectric ultrasound stimulator (ImPULS) for selective deep brain activation

by

Jason F. Hou

This thesis has been reviewed and approved by the following committee members:

THESIS SUPERVISOR

Dr. Canan Dagdeviren
Associate Professor of Media Arts and Sciences
Massachusetts Institute of Technology

THESIS READER

Dr. Edward S. Boyden
Professor of Brain & Cognitive Sciences, Media Arts & Sciences, and Biological Engineering
Massachusetts Institute of Technology

THESIS READER

Dr. Mikhail G. Shapiro
Professor of Chemical Engineering
California Institute of Technology

ACKNOWLEDGMENTS

Thank you to my group, the Conformable Decoders, and to my advisor, Canan Dagdeviren, for her unconditional support throughout the past two years through the many peaks and valleys of this project.

Words cannot express my gratitude to our collaborators across Boston Univerisity and MIT who made this work a reality. Thank you to Steve Ramirez and his students Evan Ruesch and Albit Caban-Murillo, who not only guided us in the rich intricacies of neuroscience but also stuck with us over the course of this project to pursue discovery. Thank you Kian Caplan from Fan Wang's lab at MIT for his fearlessness and curiosity in driving meaningful in-vivo experiments to elucidate the mechanisms of our device. Thank you Brandon Williams from John White's Lab at BU for his determination and thoughtfulness in running two-photon imaging and slice electrophysiology. Huge thanks for Ernesto Hidalgo and Prof. Mikhail Shapiro for hosting me at Caltech, thoughtful discussions, and for extreme efficiency in running experiments.

A major thank you to Md Osman Goni Nayeem, or Nayeem, my research mentor and coauthor, cleanroom disciple, and fellow student of life.

I also thank my thesis readers, Prof. Ed Boyden and Prof. Mikhail Shapiro, who generously provided their resources, knowledge, and expertise. Additionally, this endeavor would not have been possible without the generous support from the Media Lab Consortium, who has funded my time here.

To my lifelong friends, classmates, and cohort members, in the Media Lab and beyond. I wouldn't have made it without you all: Duncan, Kush, Jocelyn, Wazeer, and Sarah, group mates Colin and Aastha. Thank you for the moral support, late-night froyo, and Thursdays at the Muddy.

Finally, thank you to my parents Hong and Pei and my brothers Jerry and Justin. Their unconditional support and belief in me have kept me committed to pursuing my greatest dreams and aspirations.

CONTENTS

LIST OF FIGURES

LIST OF TABLES

1 INTRODUCTION

Precise and reversible spatiotemporal control of neural activity is the ultimate goal of most neurostimulation strategies both in therapeutic applications and neuroscience research. Current neurostimulation strategies can be broadly divided into two categories: i) non-invasive and ii) invasive. Some existing non-invasive methods used in clinical treatment are transcranial magnetic stimulation (TMS) [28], transcranial current stimulation (TCS) [26], and transcranial-focused ultrasound (tFUS) [9]. While these methods can avoid surgery and associated recurrent risks [53], TMS and TCS approach more specifically encounter scattering of electromagnetic energy through bone and tissue attenuation [58][12]. Unobstructed transcranial focused ultrasound (tFUS) beams can achieve millimeter-scale resolution in neural tissue and penetrate several centimeters to excite neurons by affecting mechanoreceptive and other membrane-bound ion channels [75][71][15][50]. Furthermore, the ability to quickly evaluate potential stimulation targets and adjustable parameters such as frequency and acoustic intensity make it an advantageous approach [73][27] for neurostimulation therapy in patients with conditions such as Alzheimer's disease, epilepsy, and depression. Ultrasound, when transmitted from outside the human skull, faces significant scattering and reflection from the skull's high acoustic impedance [52], which can cause off-target stimulation via conduction through bone and auditory pathways [64][18] and even traumatic, irreversible brain injury [8].

Implantable devices allow electrical and chemical modulation of the brain, leading to significant advancements in treating neurological and psychiatric disorders [49][32][6][47][57]. Electrical deep brain stimulation (DBS) can induce reversible activation of neurons but is limited by anisotropic charge transfer across the brain's ionic medium to regions proportional to the size of the electrode [43][44]. Both the charge provided by these electrodes and the sensitivity of surrounding tissue can decrease significantly over time due to biofouling and corrosion, which limits the longevity of the device [30][63][45] b). On the other hand, an optogenetics approach provides minimally-invasive neurostimulation with high spatiotemporal resolution and cell-type specificity, yet its potential for clinical translation is limited. First, the long-term safety and efficacy of opsin expression in the primate nervous system remains poorly characterized [65]

Second, the transgenic delivery of opsins requires local or systemic viral infections, which poses the risk of immunogenicity. Lastly, optical fibers produce light scattering that is difficult to minimize, posing the risk of off-target neural activation or inhibition [16]. A robust, non-genetic platform for miniaturized neurostimulation is therefore needed to fill the gap for next-generation neural interfaces to reach high standards of safety and longevity. Recently, several reports of miniaturized ultrasonic neurostimulation devices have shown that directed ultrasound energy can activate cultured neurons [34] and neurons in brain slices [66]. However, the proposed platforms are not optimized for implantation in the deep brain due to their rigid form factors, material composition, or high power requirements. Outside of implanted electrical stimulation, there remains a lack of non-genetic techniques for anatomically localized modulation of deep subcortical brain regions.

Here, we report an implantable piezoelectric ultrasound stimulator (ImPULS) that delivers acoustic energy directly and precisely to specific populations of neurons in deep brain regions. Our key findings include the design and development of a low-power, micron-scale flexible piezoelectric micromachined ultrasound transducer (30 µm thick with an outline width of 140 µm where diameter of active piezo element is 100 µm) that can evoke neurons adjacent to transducer in the deep brain. ImPULS i) utilizes biocompatible potassium sodium niobate [(K,Na)NbO_3, KNN] [17] as a piezoelectric thin-film suspended on top of an air-filled cavity to enable maximum membrane vibration for ultrasound generation of 59.2 kPa at 15 µm away from device (100 kPa adjacent to transducer), ii) remains functional after 7 days in an accelerated (75 °C) phosphate-buffered saline (PBS) solution without incurring significant electrical and mechanical degradation, and iii) does not cause temperature rise above safe tissue thresholds during ultrasound generation [75]. We demonstrate the stimulation of neurons in a coronal hippocampal slice ex vivo captured by two-photon microscopy and selective activation of neurons in the hippocampus of an anesthetized mouse to induce expression of the activity-dependent gene c-Fos. Furthermore, in vivo stimulation of dopaminergic neurons in the SNc with ImPULS elicits time-locked modulation of striatal dopamine release, demonstrating ImPULS as a powerful neuromodulatory tool.

2 BACKGROUND

2.1 ULTRASOUND NEUROMODULATION

Targeted ultrasound neuromodulation has the potential to revolutionize neuroscience and transform the treatment of neurological and psychiatric disorders. In neuroscience research, it has been used to investigate the underlying mechanisms of neural function, as well as explore the diverse biological machinery that sensitizes neurons to forces like ultrasound. In the clinical setting, ultrasound neuromodulation has the potential to provide non-pharmacological and non-invasive treatments for a range of neurological and psychiatric disorders, such as epilepsy[37], depression[21], and Parkinson's disease[35]. Modulation of neurotrophic factors in the hippocampus following ultrasound stimulation [40] raise insights into whether ultrasound can provide more than excitation or inhibition, and also be used to encourage plasticity or neuroprotective effects for the treatment of neurodegenerative disorders. Finally, the use of ultrasound to deliver therapeutic agents to the brain, such as drugs or gene therapies that make use of sonogenetics[23], is an area of active research with promising results[41].

2.1.1 Mechanism

The effect of neurostimulation from focused ultrasound produced from external transducers has been shown to provide robust activation in cultured neurons, slices, and in live mice [34][15][75][66]. So far studies have found various components of neural cells to contribute to the effect of ultrasound-mediated neurostimulation including transient receptor potential channels such as TRPA1[50] and TRPV4[39], K+ channel family TREK-1, TREK-2, and TRAAK [33], mechanosensitive channels including Piezo1 and Piezo2[56], as well as the modulation of Sodium and Calcium ion channels [75][72]. Other neural cells such as astrocytes occupy most of the volume in neural tissue, serve as the contact between primary neurons and vascalature, and have also been found to significantly contribute to the neuromodulatory effect[50]. As ultrasound waves propagate through tissue, energy is dissipated as heat in viscous frictional forces

and through elastic deformation of the tissue itself. This deformation of the cell membrane can alter membrane capacitance or induce membrane polarizations from strain gradients, leading to a rise in excitability [51]. Furthermore, the adiabatic soliton theory proposes that mechanical pulses accompany action potential propagation, which could be stifled or enhanced by afferent or efferent ultrasonic forces[22], respectively. The compound physical mechanisms of ultrasound activation of cells within neural circuits must be investigated in a controlled and chronic manner with the awareness for off-target activation, such as through the auditory pathway[64][18]. However, robust activation of neural tissues have consistently been demonstrated and further explored for therapeutic uses.

2.1.2 Stimulation Parameter Space

Ultrasound frequencies in the range of 0.2-3 MHz have shown to have neuromodulatory effects in the central nervous system (CNS) in cells, slices, and in-vivo[74]. With higher frequencies, higher pressures are necessary to acheive neural excitation. High frequencies >3 MHz produce larger acoustic radiative forces (ARF) but have lower cavitation thresholds, and even frequencies up to 43 MHz have shown to stimulate retinal cells[46]. Finally, ultrasound stimulation of different frequencies has been reported to produce either excitatory or inhibitory [19][10] effects to target tissues, suggesting that these effects can be controlled with the proper targeting and choice of stimulation parameters.

The intensity or pressure of ultrasound waves can be titrated to produce different physical effects. One type of device is the focused ultrasound (FUS) system, which uses high-intensity ultrasound waves to target specific regions of the brain and induce focal changes in brain activity and shown to be effective in treating essential tremor through thermal ablation and selective lesioning of tissue. Another is the transcranial ultrasound (TUS) system, which emits lower-intensity ultrasound waves that can penetrate the skull and reach deeper structures. TUS has been used for both research and therapeutic purposes, and has shown promising results in treating conditions such as depression and chronic pain. These pressure waves cannot exceed FDA safety limits on intensities of 720 mW/cm^2 for clinical applications. Typically, pressures exceeding 100 kPa have shown to produce neuromodulatory effects in the CNS[75].

Pulse repetition frequency (PRF) can be configured to reduce the overall time the transducer is on during a stimulation duration, which reduces power

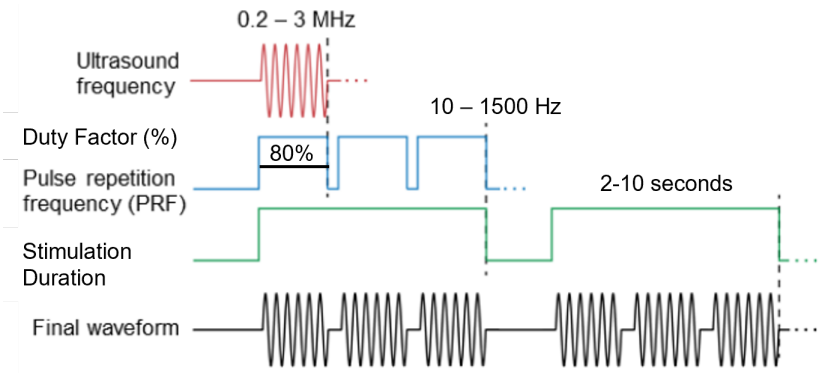

Figure 1: Visual representation of ultrasound stimulation parameters in a single waveform.

consumption and heat generation. As opposed to a continuous wave (CW), pulsed wave stimulation have been demonstrated more successfully with PRFs in the 300-1500Hz range[42].

2.2 ULTRASOUND TRANSDUCERS

There are various types of ultrasound emitting devices that are used for neuromodulation, each with unique features and capabilities. Ultrasound transducers are devices that emit ultrasound energy with the application of external energy such as electricity or light. Common types of ultrasonic transducers include those made of bulk and thin-film piezoelectric materials, optoacoustic emitters, and electrostatic-based transmitters. These various methods of generating ultrasound energy have further trade offs in their ease of fabrication, scalability, and cost.

Recently, a new class of transducers has been reported and used for neurostimulation applications. Optoacoustic transucers use the photoacoustic effect to convert an incident laser beam confined in a tapered optical fiber to thermal energy after striking a light-absorbing material causing shock waves of expansion[66]. With short pulses occupying tens of nanoseconds, these devices can avoid excess heating and produce pressures >1 MPa in a a confined area less that 100 µm in diameter. While these devices have shown great promise in driving new cellular-scale experiments in ultrasound stimulation, they cannot be produced with high scalability, require an expensive laser source, and have limited durability after repeated actuation.

In the case of piezoelectric materials, transducers are typically made using machined bulk piezoceramic materials that are subtractively manufactured using wafer dicing saws, diamond wires, or short pulse-width lasers. Piezoceramic materials have high durability and can be acutated for billions of cycles with minimal loss in performance[70]. Following dicing of individual elements, interconnections to the top and bottom sides of the piezoceramic and a matching and backing layer must be bonded to improve electromechanical coupling efficiency. Often, these steps are manual, have low repeatability, and add rigidness and bulkiness to the overall device.

Devices such as capacitive micromachined ultrasound transducers (CMUTs) and piezoelectric micromachined ultrasound transducers (pMUT) use thin-film membranes suspended over an air-filled cavity. While CMUTs use electrostatic attraction and high voltages (>20V) to actuate the membrane, PMUTs use the inverse piezeoelectric effect to convert alternating voltage into actuation. As single elements, pMUTs can be driven with smaller voltages (<20V) to produce comparable ultrasound pressures. Both CMUT and pMUT devices have been successfully manufactured at scale in MEMS foundries for commercial applications and capitalize on existing standard fabrication process to produce high-throughput and high-yield production runs. With existing silicon-substrate processes, these devices are also planar and bulky, but have the potential to be thinned down for flexibility in Back End-of-Line processing or fabricated on flexible substrates as is shown in this work.

Subcortical Ultrasound Neurostimulation Devices					
Device	**Resolution in deep tissue (<5mm)**	**Max Pressure**	**Power Consumption**	**Size**	**Safety**
Transcranial Focused Ultrasound (tFUS)	1mm	10MPa	5W	External focused transducer	Non-invasive
tFUS with cranial window	<1mm	10MPa	5W	External focused transducer	Requires craniotomy
Optoacoustic tapered fiber[66]	<100µm	4MPa	>50W	Microscopic fiber & large laser source	Requires craniotomy & fiber implant
Silicon pMUT[34]	100µm	400kPa	100uW	mm2 sized arrays	Requires craniotomy & implant
This work (ImPULS)	<100µm	200kPa	2mW	Micron sized	Requires craniotomy & implant

Table 1: Table comparing the various techniques and devices used to achieve ultrasound neurostimulation in subcortical regions.

3 DESIGN AND FABRICATION OF IMPULS

3.1 OVERVIEW

The implantable piezoelectric ultrasound stimulator, ImPULS, is a flexible piezoelectric micromachined ultrasound transducer (pMUT), that is surgically implanted into the brain. A schematic of the ImPULS implanted into a subcortical region of a wild-type mouse is shown in Figure 2.

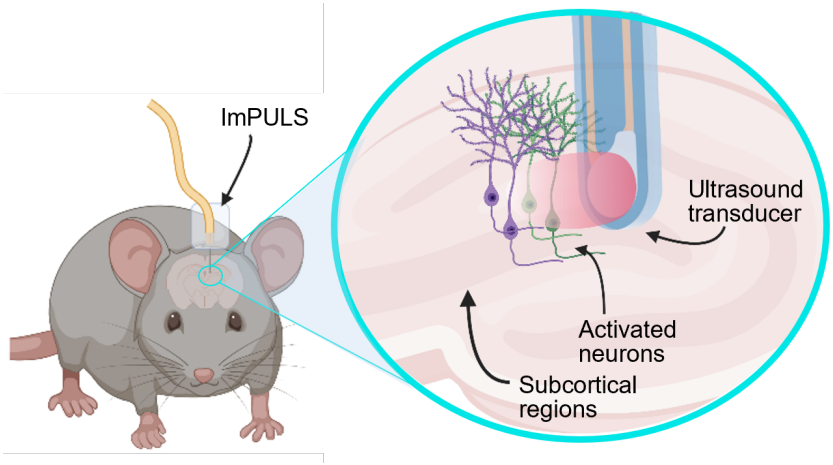

Figure 2: Schematic illustration of an implantable piezoelectric ultrasound stimulator (ImPULS) implanted in a subcortical brain region of a wild-type mouse. A magnified view showing the activated neurons with ultrasound application.

Upon application of an alternating voltage, ImPULS generates an ultrasound beam and excites nearby neurons as described in detail in later sections. The fabrication of the ImPULS device introduces a new transfer printing process of lead-free KNN piezoelectric thin films onto biocompatible polymer substrates. This involves wet etch patterning and release of target films from host wafers and integration onto polymer SU-8 by transfer printing as seen in appendix Figure 31. The substrates can be engineered to serve the requirements of the application such as chemical resistance, stiffness, and biostability. Because ImPULS is microfabricated using conventional cleanroom technologies, it can

be manufactured at scale and with high cost efficiency and operated with low power requirements.

3.2 IMPULS DEVICE STRUCTURE

Each comprising layer of ImPULS can be visualized in a peeled-view in Fig. 3 comprising SU-8 as substrate (0.8 µm in thickness), encapsulation and backing layers (0.5 µm and 15 µm in thickness, respectively); piezoelectric KNN layer (1 µm in thickness, and 100 µm in diameter); chromium/gold (Cr/Au, 10/250 nm in thickness) and platinum (Pt, 100 nm in thickness) serving as top and bottom electrodes, respectively and Cr/Au as metal interconnects (10/250 nm in thickness). We chose to design the pMUT with a pinned boundary device structure in order to maximize the vibration amplitude of the active membrane [38]. In order to fabricate a free-standing membrane suspended over an air-filled cavity, we fabricated the devices in an inverted manner, which included a final bonding of a backing layer and exposure through a thin transparent PET layer to seal the cavity. The cavity and backing layers are also designed to improve the stiffness of ImPULS for acute implantation without an insertion shuttle.

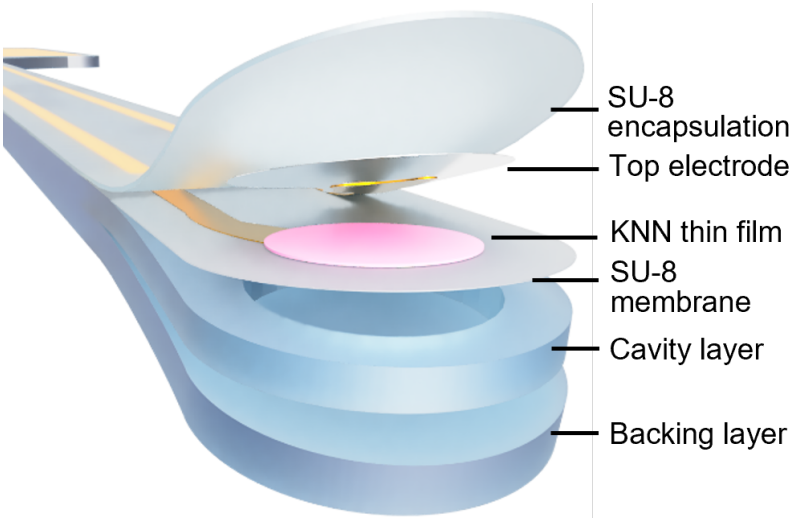

Figure 3: Schematic of a peeled view of ImPULS, revealing each layer. The ImPULS is a piezoelectric micromachined ultrasound transducer (pMUT) structure where biocompatible potassium sodium niobate (KNN) is sandwiched between two thin SU-8 layers, and an air-filled cavity and a backing layer is formed underneath the piezoelectric thin-film membrane.

We choose KNN as the lead-free piezoelectric layer due to i) its comparably high piezoelectric coefficients (e31, d31) and durability (DC stress lifetime: >24 h at 200 °C and 30 kV/cm, and Curie temperature of 350 °C) that exceeds commercially available doped lead zirconate titanate (PZT), ii) its proven biocompatibility and non-toxicity [17][4], and iii) its commercial availability, and ability to be processed using simple cleanroom microfabrication processes. The initial P-E characteristic of KNN before fabrication is shown in fig. S3.

The microfabricated unit is connected to a custom-designed printed circuit board (PCB) using an anisotropic conductive film (ACF) based cabling to complete the final device fabrication (Fig. 1C). Heat-press using a solder tip at 180 °C ensured conformal bonding between cable and contact pads of both the device and PCB, which was further confirmed using a multimeter and electrical impedance spectroscopy. The ACF cable was then finally encapsulated using Kapton tape.A colorized scanning electron microscopy (SEM) image of the cross-section of ImPULS shown in Fig. 1D depicts the air-filled cavity and encapsulation of the active electrical elements.

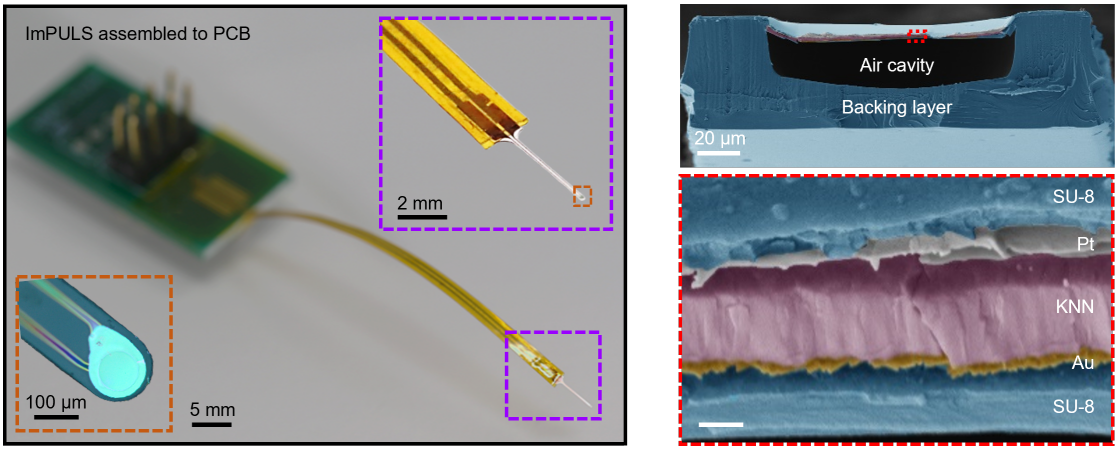

Figure 4: (Left) Optical image of ImPULS assembled with flexible ACF cable and a custom printed circuit board (PCB) with a magnified view of the ImPULS probe (top inset) and further zoomed version of the tip of probe under a microscope (bottom inset). (Right) Colorized cross-sectional scanning electron microscope (SEM) image of ImPULS showing its compositional layers.

3.3 FINITE-ELEMENT SIMULATION

To understand the effect of device structure geometries on the resonant frequency and pressure beams of our custom pMUT transducers, we performed acoustic simulations in a water medium using finite element analysis (FEA) in COMSOL Multiphysics. The materials properties of KNN used for simulation are used as follows: density of 4000 kgm^{-3}, Young's modulus of 65 GPa, relative permittivity of 1500, piezo constant of e_{31} 12 Cm^{-2} [29] . The model uses 'finer' mesh and solves the pressure acoustics, electrostatics, and solid mechanics physics for the solution. The geometry of the model matches the dimensions of experimentally measured geometries.

The membrane vibration dynamics were visualized with the OnScale Solver to evaluate residual stress concentrations between layers in the piezoelectric membrane stack.

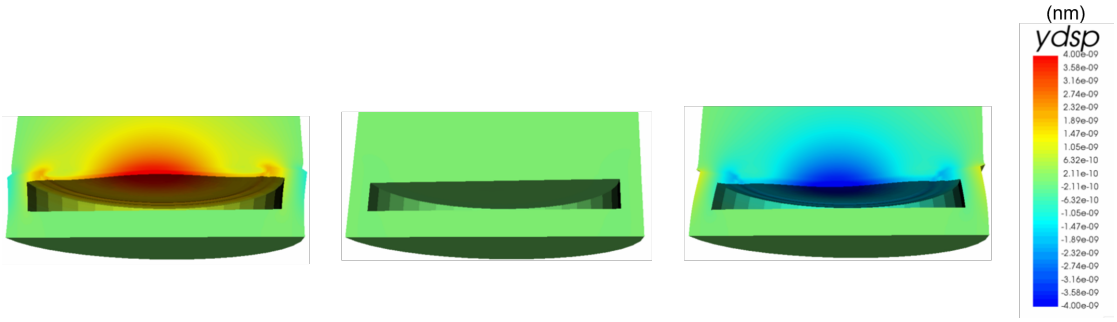

Figure 5: Simulated membrane dynamics in water medium during piezoelectric actuation.

As shown in Fig. 6, the maximum pressure adjacent to the transducer can reach 100 kPa, which decreases gradually following a spherical pressure distribution. In these simulations, the near-field pressure region lies within 2 microns of the transducer surface and generates ultrasonic pressures in the far-field within reported ranges for neurostimulation within 20 µm.

The resonance frequency of the device when submerged in water or implanted has a pronounced but consistent downward shift due to the hydrostatic forces exerted on the flexible material surrounding the entire device and the piezoelectric thin-film itself [54][68] that affect the intrinsic tensile stress within the device structure. Resonant frequencies were found to have a strong, mostly-

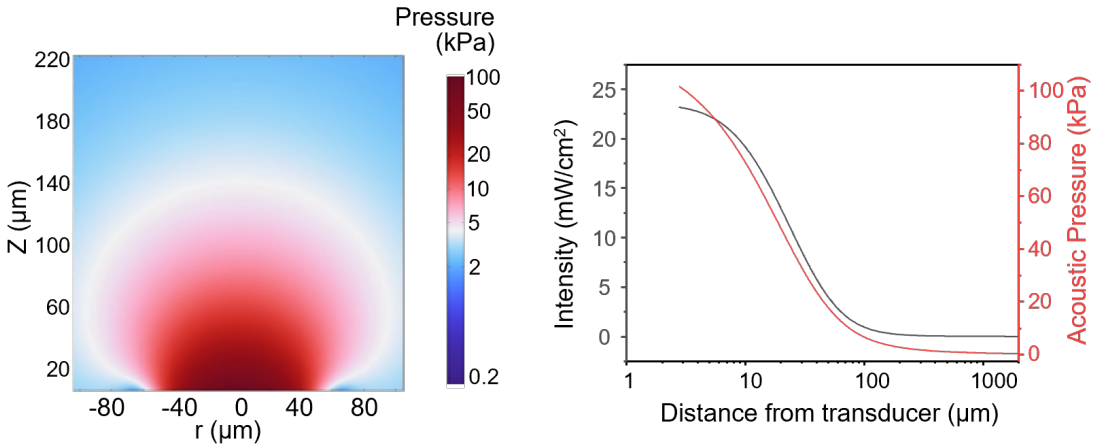

Figure 6: (Left) View of the acoustic pressure from the side profile of ImPULS. (Right) Simulated acoustic pressure and power profiles of axial line normal to the center of the transducer.

linear dependence on cavity width, although is also a function of membrane stiffness. The resonant frequency of a pMUT device can be determined as

$$f = \frac{\alpha}{2\pi r^2}\sqrt{\frac{D_E}{\rho h}} \tag{1}$$

$$D_E = \frac{Eh^3}{12(1-\nu^2)} \tag{2}$$

where α is the resonance mode constant, r is the radius of the cavity, D_E is the flexural rigidity, ρ is the effective density of the membrane, h is the membrane thickness, E is the effective Young's modulus, and ν is Poisson's ratio [55]. When the intrinsic stress is high, it can dominate the flexural rigidity and increase the resonant frequency.

The multiphysics model also allows us to estimate pressure ranges based on the maximum central displacement of the membrane. In later sections, measurements of displacement and pressure will be compared to simulated values to validate the results of the simulations.

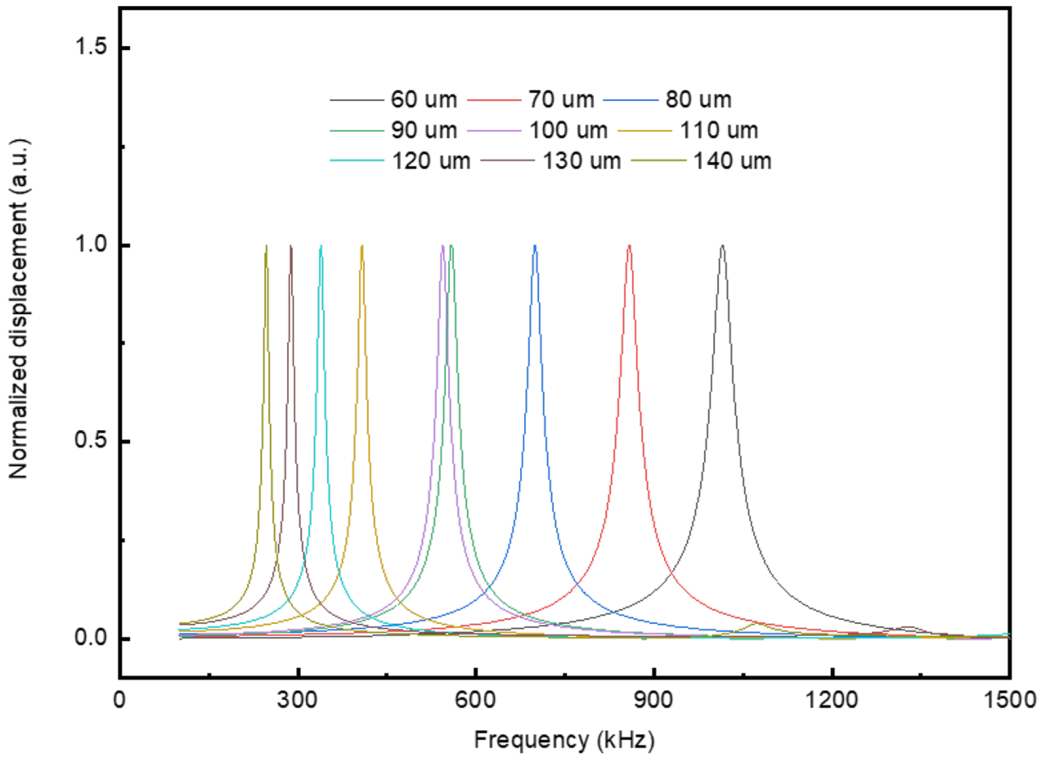

Figure 7: Simulated frequency spectra of different pMUT structures with varying cavity diameter.

3.4 MICROFABRICATION PROCESS DESCRIPTION

A starting thin-film stack of 500 nm SiO_2/ 610 µm Si/ 500 nm SiO_2/30 nm ZnO/ 200nm Pt/ 1 µm KNN/ 10nm Cr/150nm Au on a donor wafer (SCIOCS Co. Ltd., Sumitomo Chemical Group, JAPAN) was processed in preparation for transfer printing. Contact photolithography (Karl Suss MJB4) with spin-coated positive i-line photoresist (PR) (Microchemicals AZ4620) of 15 µm thickness was used to define wet etching patterns for top and bottom electrodes and the piezoelectric transducer. Top electrode Au and Cr layers were wet etched with gold etchant (Transene) and CR-7 chrome etchant (Transene), respectively. KNN was subsequently defined using the same photoresist mask and wet etching with 49% hydrofluoric acid (HF). We introduce an alternative acidic wet-etching chemistry for KNN patterning that can achieve faster etch rates of up to 100

nm/min etch rate, which mediates the undercut effect and allows for denser and smaller transducer pitches. Typically, KNN is etched in

PR was then stripped in a 120 °C heated NMP-based stripper (Microchem AZ400T). The Pt bottom electrode pattern was defined with a PR etch mask (AZ 4620) and both ZnO/Pt were dry etched using reactive-ion etching (RIE) flowing Ar/O2 (95%/5%) and power of 500W (Plasmatherm). A final single PR layer was designed to both preserve element-to-element alignment and serve as a mechanical support during undercutting, release, and transfer printing. The thin film stack was finally undercut with a diluted hydrogen fluoride (HF) solution with a weight ratio of 49%/60%: HF/Deionized (DI) water, rinsed, and delaminated from remaining thermal oxide using thermal release tape (Revalpha 90 °C). This anchor-layer step is crucial to maintaining relative spacing of elements during the HF undercut. We designed a special anchor modifying our previously reported recipe [7] extend processing window and mechanically support the pattern with of PR, ensuring high yield in the transfer to thermal tape (see fig. S2 for details). The patterns were transferred to the tape and prepared to be printed on a SU-8 (Kayaku Advanced Materials) flexible substrate. Several examples of higher channel and density linear and 2D arrays in various steps of device fabrication are shown in Figure 9.

A separate substrate Si wafer was coated with an Omnicoat (Kayaku Advanced Materials) release layer, followed by a 0.5 µm thick layer of SU-8 2000.5. The wafer was then soft-baked and flood exposed for 2 s with 365 nm ultraviolet (UV) light. The collected pattern on the thermal release tape was then pressed onto the substrate and left on a hotplate to slowly heat up to release temperature during the post-exposure bake of the SU-8. Finally, at the release temperature, the tape was gently removed with tweezers and the PR anchor was removed with sprayed acetone and 2-propanol. Following a short RIE O2 plasma treatment, an insulation and opening layer of SU-8 was spun onto the wafer and patterned to leave opening contacts to the top and bottom electrodes for metallization and metal interconnects to bondpads. The entire structure was then hard baked at 120 °C to ensure proper adhesion between layers and reduce the angle of the sidewalls around the metal contact openings to ensure proper connectivity after metallization. 10 nm of Cr and 200 nm of Au were deposited over the entire substrate and patterned with a PR mask for wet etching to define the metal interconnects and larger bond pads that will allow the device to be connected to external instrumentation. After the device is rinsed and resistivity of the resulting surface is checked to ensure complete etching of conductive material, the device is stripped of PR, cleaned, dried with N2 spray gun and treated with O2 plasma preceding deposition of the next insulating layer. Next,

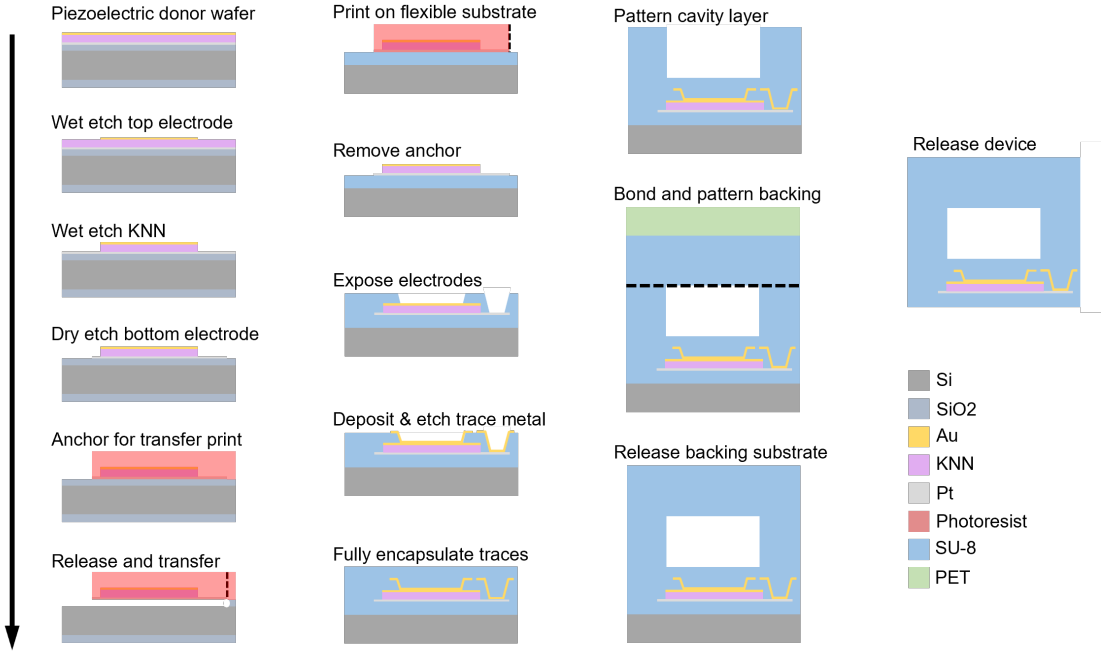

Figure 8: Schematic illustration of the main microfabrication steps of ImPULS.

a 0.5-0.8 µm thick layer of SU-8 is spun, exposed, and cured to complete the insulation of the electrically active elements.

The cavity layer is a thicker mechanical layer (ĩ5 µm) that can be designed to control the resonant frequency of the device. The dimensions of the cavity determine the resonance frequency [55]. Implants require sufficient stiffness for ease of surgical implantation without the need for an insertion shuttle. We fabricated a SU-8 backing layer of 15 µm to give the device sufficient stiffness while maintaining the overall flexibility of the structure. First, a thin layer of polyvinyl alcohol (PVA) (4 wt%) was spin-coated to a polyethylene terephthalate (PET) film at 3000 rpm for 45 s followed by an annealing process of 10 min at 110 °C. This PVA layer works as a sacrificial layer to aid the delamination of the PET backing during development. Following a short RIE O_2 plasma treatment, SU-8 2050 was spun at 6000 rpm for 45 s. The sample was then soft-baked for 5 min at 65 °C followed by 5 min at 95 °C in order to achieve an appropriate surface for bonding. The previously prepared wafer with the cavity layer and the rest of the device structures were then bonded to the SU-8 on PVA and pressed gently. The final pattern which defines the device perimeter was then exposed through the PET film to seal the cavity layer and served as a final layer

to stiffen the device. After post-exposure bake, the bonded substrates were soaked briefly in 2-propanol to dissolve the PVA sacrificial layer. Finally, the unexposed SU-8 was developed.

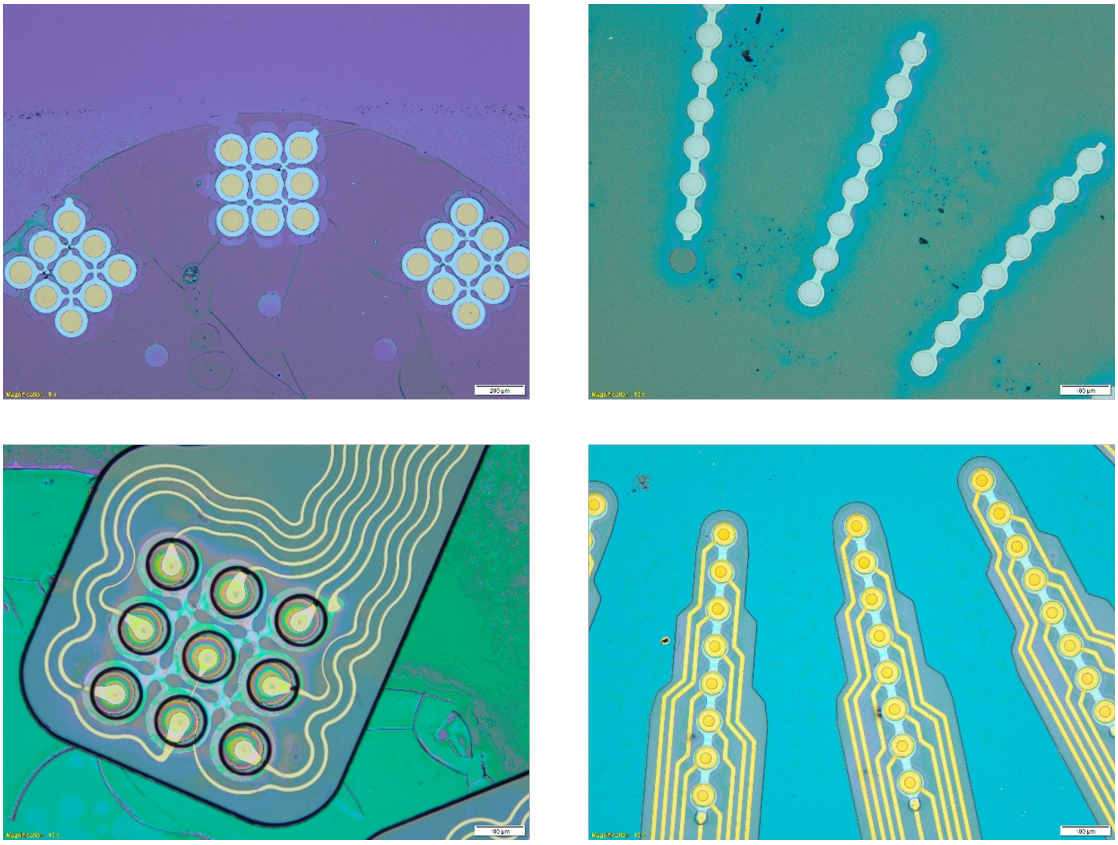

Figure 9: Multi-element transfer-printed arrays in various steps of fabrication. Scale bars (100µm: top left, top right, bottom right, 200µm: bottom left

In order to release the devices from the wafer substrate, the bottom-most layer of SU-8 was blanket dry-etched in CF_4/O_2 for a min to expose the initial Omnicoat layer and release the devices. Once the SU-8 was exposed, the devices were immersed in MF-26A developer (Kayaku Advanced Materials) and undercut by the dissolving Omnicoat layer until they were released. The devices were allowed to soak for 45 min for the Omnicoat to dissolve completely and were then rinsed in 2-propanol and DI water until clean. The devices were collected and arranged under a final shadow mask and dry-etched to expose the metal bond pads, which were used to connect the microfabricated component to the PCB.

4 CHARACTERIZATION OF IMPULS

To optimize the device parameters systematically, the electromechanical, acoustic, and durability properties of ImPULS were investigated. This next section summarizes the tests performed to validate the performance of the ImPULS device as well as some of the findings that were useful in improving the device.

4.1 PIEZOELECTRIC PROPERTIES OF KNN

The KNN characterization curve was measured by Sumitomo Chemicals Co. (Japan) to assess the hysteresis loop and quality of the piezoelectric material. The plot in Fig. 10 shows that there is a balanced exchange of current in forward and reverse polarization, illustrating the quality of the films [67].

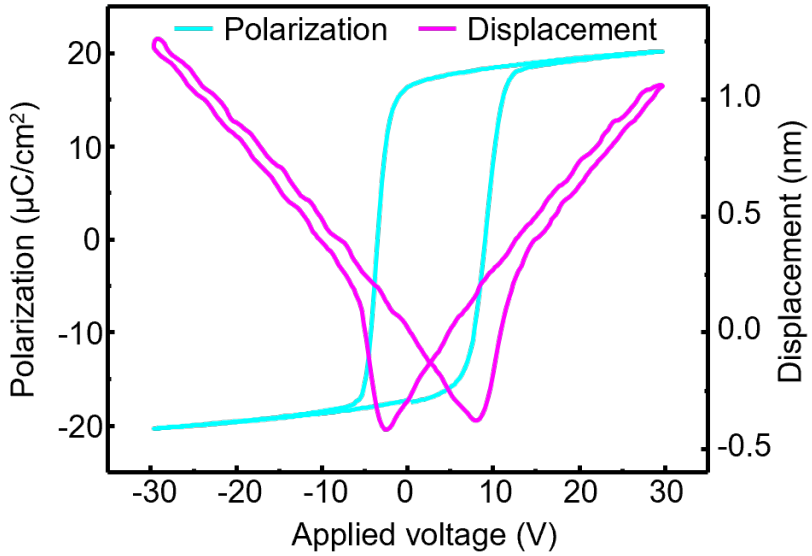

Figure 10: P-E hysteresis loop and piezoelectric displacement butterfly loop of KNN measured on donor wafer.

4.2 ELECTRICAL IMPEDANCE SPECTROSCOPY & TRANSDUCER POWER CONSUMPTION

The electrical impedance and phase angle spectra of the ImPULS measured in air and water medium are shown in Fig. 11. Accordingly, we observe consistent decreases in resonance frequency of 40.4%, from 840 kHz to 500 kHz, in air versus water mediums, respectively.

An impedance analyzer (E4990A, Keysight Technologies) was used to characterize the electrical impedance spectrum to determine the resonant frequency in both air and water mediums. In order to measure the impedance characteristics of the microfabricated device alone, the system was calibrated to probe tip terminations that were used to contact a Gallium Indium eutectic (Sigma Aldrich) liquid-metal bridge extending from the contact pads of the device.

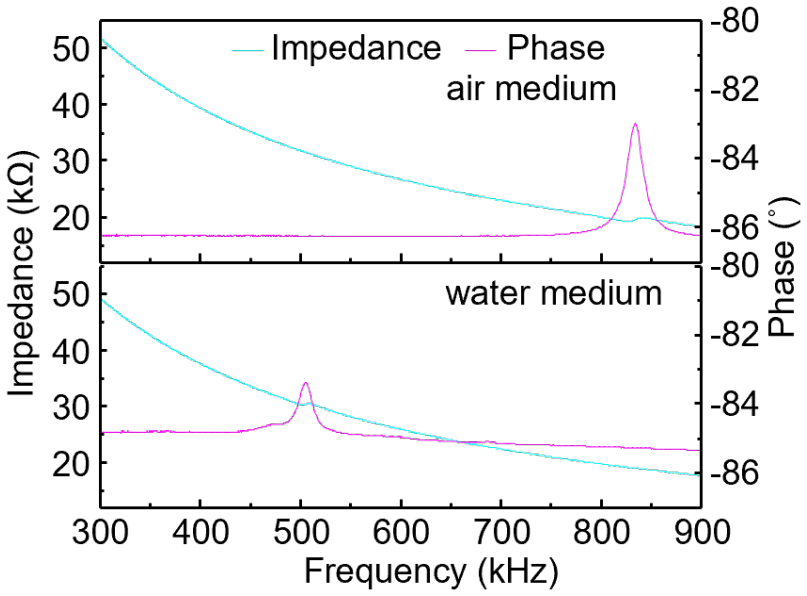

Figure 11: The impedance and phase angle spectra of ImPULS at air and water medium, showing the resonance frequency in both mediums. (B) Displacement of ImPULS at air and water medium measured using laser doppler vibrometer (LDV) when the inputs are periodic chirp (bottom) and sinusoidal signal (top).

The power consumption of ImPULS can be determined through impedance measurements of the assembled device at the resonance frequency and the voltage applied through the following equation:

$$P_{avg} = \frac{1}{2} V_{max} I_{max} cos(\theta_i - \theta_v) \tag{3}$$

With 10 V(p-p), the ImPULS device without cabling consumes 1.3 mW of power, making it a highly efficient device. With the addition of extra the extra ACF and PCB, the cable capacitance adds additional impedance, which reduces the current flowing through the active elements.

4.3 ELECTROMECHANICAL CHARACTERIZATION

The displacement amplitude of device was measured using a Laser Doppler Vibrometer-based non-contact vibration measurements (LDV, MSA-500, Polytec). The LDV is able to capture the frequency spectrum of vibration displacement and velocities generated by the piezoelectric transducer. ImPULS was mounted on a two-axis chuck. Different driving signals were applied to the device using the system's internal function generator. First, the different resonant modes were determined by applying a periodic chirp signal excitation ranging from 100 kHz to 2 MHz. Later, a pure sinusoidal signal is applied at the resonant frequency to measure the maximum vibration amplitude. This experiment was conducted in both air and water mediums. A displacement of 137 nm at a

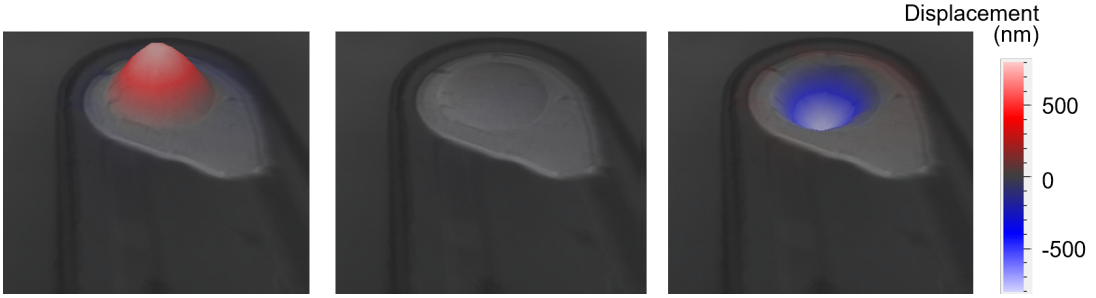

Figure 12: Three representative stages of membrane vibration upon application of sinusoidal signal at fundamental resonance frequency.

resonance frequency of 840 kHz (air medium) and displacement of 230 nm (water medium) was achieved upon application of a 4 V (p-p) sinusoidal signal.

The movement and shape of membrane deformation can be visualized from a 3-D reconstruction of the 2-D scan as shown in Fig. 12.

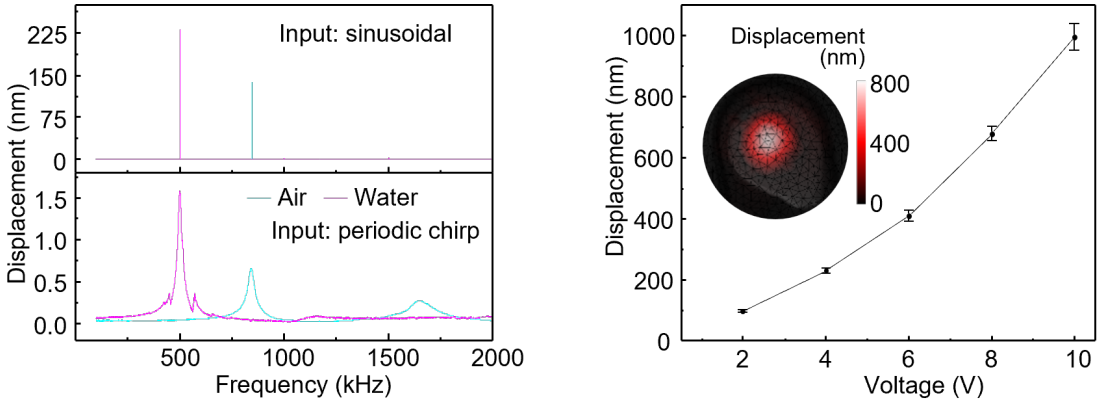

Figure 13: (Left) Displacement of ImPULS at air and water medium measured using laser doppler vibrometer (LDV) when the inputs are periodic chirp (bottom) and sinusoidal signal (top). (Right) Displacement of ImPULS as a function of input voltage (p-p) with inset showing two-dimensional (2-D) point scan of displacement indicating the lateral resolution of beam pattern of the device. Error bar represents standard deviation in measurement, N = 3.

The pressure output of pMUT structure is proportional to the center displacement of the vibration plate, and the center displacement represents the point of maximum mechanical energy transduction[38]. To optimize the device performance, we fabricated the ImPULS with different cavity sizes. As shown in Fig 13, the resonance frequency decreases with the increase in cavity diameter. It has been reported that the most significant modulation of neurons occurs with the application of ultrasound at frequencies less than 1 MHz (ref a b). We, therefore, choose to characterize devices with a cavity size of 105 µm that has a resonance frequency of 500 kHz. To investigate the effect of applied voltage on the transducer, we varied voltage from 2 V to 10 V (p-p) and recorded the peak displacement using a laser doppler vibrometer (LDV) in both air and water mediums. As shown in Fig. 13, the output peak displacement increased from 98 nm to 995 nm when the applied voltage changed from 2 V to 10 V. A two-dimensional (2-D) point scan of the displacement was used to characterize the lateral resolution of the focal point, which reaches max intensity within an 80 µm diameter (Fig. 13, inset). Notably, the increase in cavity size leads to higher displacement as shown in Fig. 14, which can be attributed to the reduced piezoelectric diaphragm stiffness with the increased cavity size.

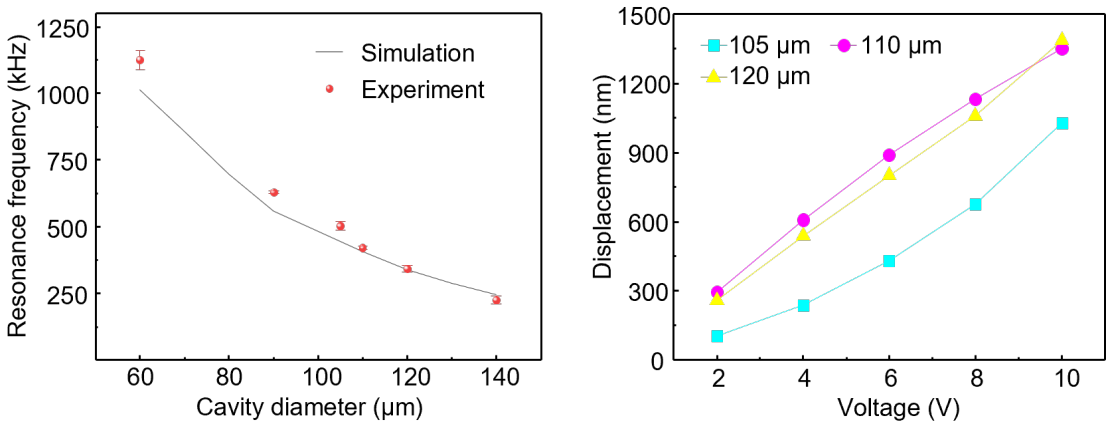

Figure 14: Effect of cavity size on resonance frequency and displacement of device.

4.4 ACOUSTIC AND THERMAL CHARACTERIZATION

We measured the pressure generated by ImPULS using a fiber-optic hydrophone. ImPULS, with a diameter of 100 μm and 1 μm thick piezoelectric thin film, creates a near-field pressure within 10 μm and far-field spreads around 100 μm in length. The electromagnetic interference (EMI) generated by the wires and piezoelectric at distances less than 100 μm degrades the sensitivity of conventional piezoceramic hydrophones and overpowers the signal of interest. Therefore, we utilized a fiber-optic hydrophone mounted on a 3-axis stage that can bypass the electromagnetic coupling effect as an orthogonal measurement modality. As shown in Fig. 15, we measured the pressure generated by ImPULS at four different distances. The experimentally measured pressure matched well with the simulated pressure values. The slight discrepancy can be attributed to unknown true position of the sensing element in the fiber hydrophone tip. Next, we scanned the fiber-optic hydrophone in x and y directions with a step size of 25 μm, keeping the z-distance constant at 15 μm. Fig. 15 shows the pressure profile mapping, where maximum pressure of 59.2 kPa is achieved at the center of the ImPULS. This characterization is important for verificatiation of precise and localized stimulation of neurons residing within the pressure field of the device.

The acoustic characterization was performed by measuring the pressure emitted from ImPULS using a fiber-optic hydrophone system (Precision Acoustics), based on the detection of acoustically- and thermally-induced thickness changes in a polymer film Fabry–Pérot interferometer deposited at the tip of a

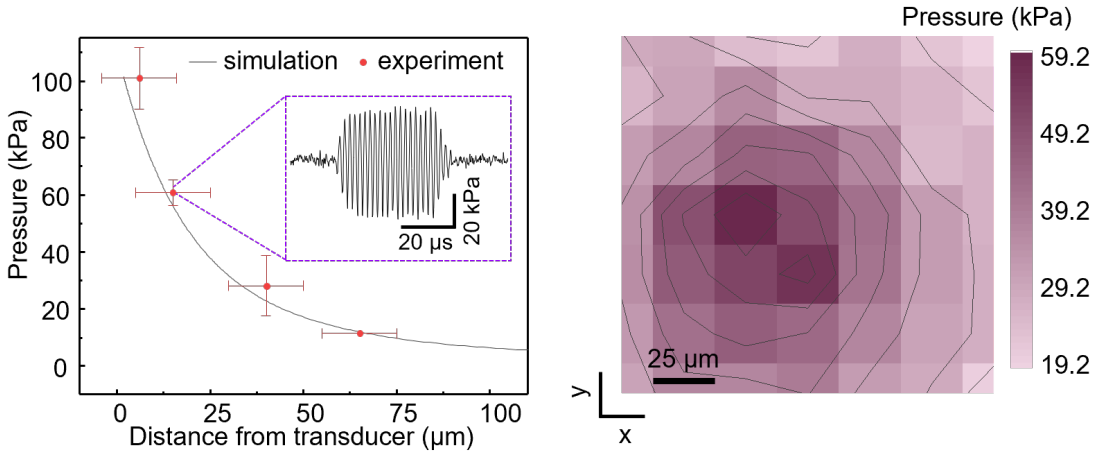

Figure 15: Comparison of simulated and experimentally measured pressure using a fiber optic hydrophone at different distances. Error bar represents standard deviation in measurement, N = 3

single mode optical fiber. which uses a Fabry-Perot interferometer to obtain both pressure and temperature change at the sensor tip, thusThis system enablesing simultaneous temperature and pressure measurements across a circular sensing area of 100 μm in diameter. The ImPULS was driven by a benchtop function generator (BK Precision Agilent) with a 20V pulsed sequence.

In order to perform a 2-D mapping of pressure and temperature across the surface of the device, the fiber optic hydrophone was mounted to a 3-axis micromanipulator (Newport), and the tip was directed into a petri dish containing deionized and degassed water at 22 °C. The ImPULS device was fixed to the bottom of the dish. Under microscope magnification, the tip of the hydrophone was steered into view and aligned on top of the device as seen in Fig. 16. The manipulator was advanced using manual manipulators and distances were measured using the microscope images taken during the experiment. After the hydrophone was driven into position, ImPULS was turned on, and the generated voltage waveform from the hydrophone was collected by oscilloscope (Agilent, 100MHz 4GSa/s) at each location.

Axial pressure measurements were conducted in an identical setup with ImPULS rotated 90 degrees about its longer axis. Therefore, when the hydrophone tip was manipulated to the vicinity of ImPULS, it was oriented to take pressure measurements in a direction normal to the active surface of the ImPULS device. We then manually advanced the device away from the hydrophone in plane, measured distance with magnified images taken by a microscope camera

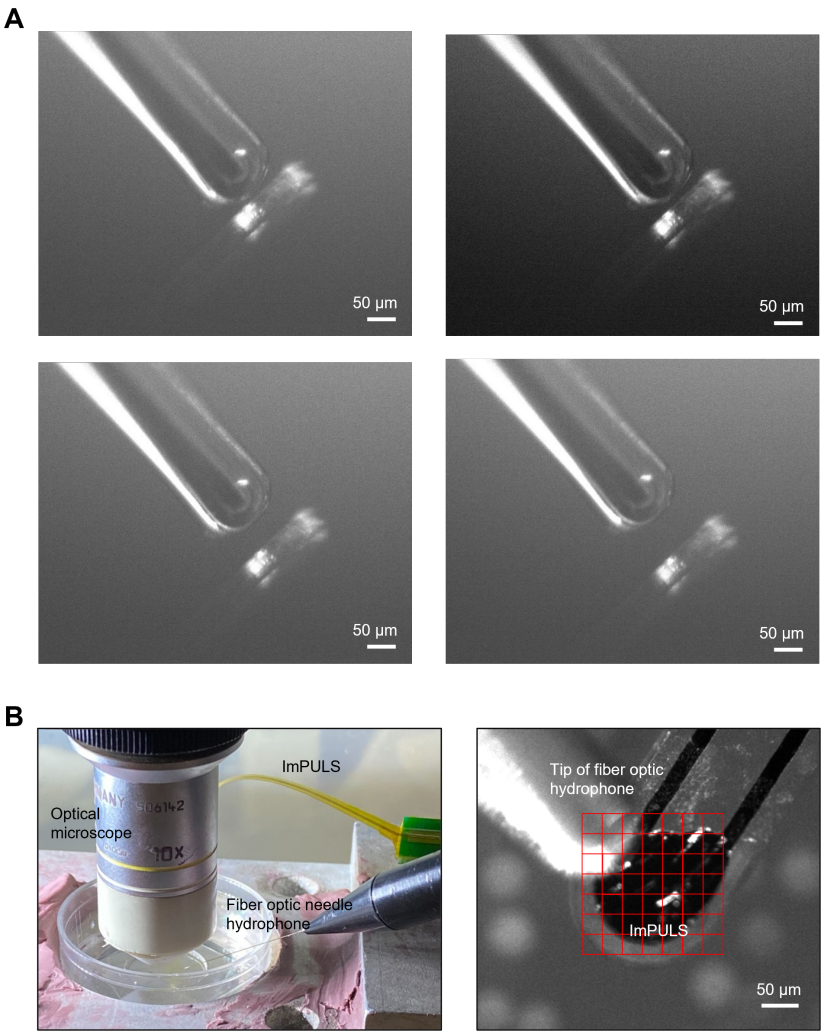

Figure 16: (A) Microscopic image (10x magnification) for pressure measurement showing four different distances between the probe tip and fiber hydrophone. (B) Setup for 2-D pressure and temperature mapping (left) and corresponding microscopic image (10x magnification). The red grid represents the approximate measurement position of fiber hydrophone.

mounted above the device and hydrophone and took a series of pressure measurements. We approximated an error margin in the measured distance due to the partial occlusion of the sensing area on the hydrophone (Fig. 16).

4.5 THERMAL STUDY

Ultrasound generation from a transducer results in a temperature rise in the surrounding medium due to the intrinsic heating of the piezoelectric. Piezoelectric transducers heat up over time due to energy loss within the material caused by internal friction resulting from applied voltage, frequency of vibration, and mechanical and electrical losses [2]. We measured changes in temperature in a water medium during ultrasound application using a dual sensing fiber-optic hydrophone capable of simultaneous measurements of acoustic pressure and temperature at the same location[48]. The . The fiber optic thermometer positioned 15 µm away from the transducer recorded a temperature rise upon application of continuous ultrasound waves.

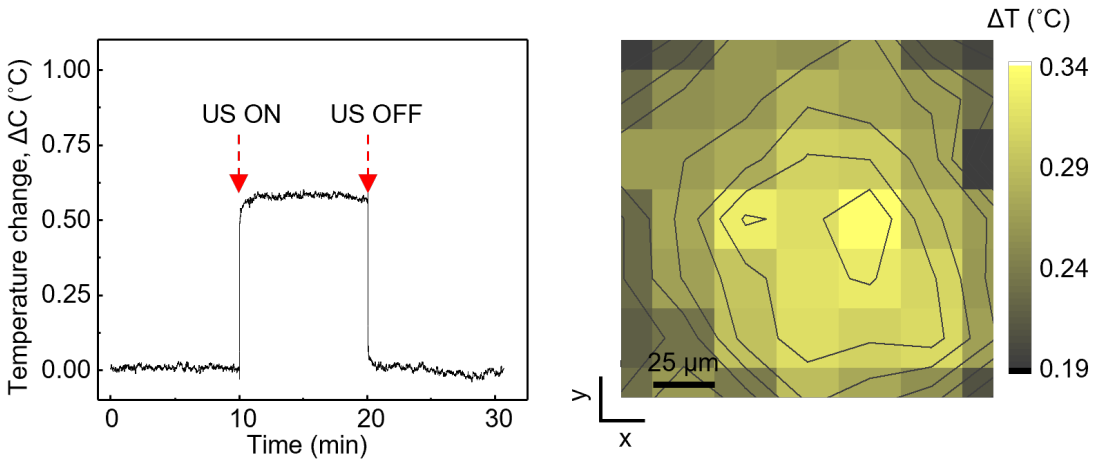

Figure 17: (Left)Temperature change in water medium when a continuous sinusoidal signal of 500 kHz at 20 V (p-p) applied to ImPULS. Ultrasound was 'off' for 10 min, 'on' for 10 min and 'off' for 10 min. (Right) 2-D mapping of temperature generated by ImPULS measured at z = 15 µm.

As shown in Fig. 17, 10 min application of continuous sinusoidal signal at an input voltage of 20 V (p-p) gave rise to only 0.6 °C which is much less than the threshold of temperature-evoked neuromodulation [3][75] . In practical neurostimulation applications, thermogenic effects are further reduced without affecting peak pressures generated due to the application of a pulsed ultrasound signal instead of a continuous signal. Further, we measured the temperature change upon application of pulsed signals with duty cycles of 50% and 5%. As shown in Fig 18A and 18B, application of 50% and 5% duty cycle pulsed

waves gave rise to only 0.15 °C and 0.03 °C respectively. The dependence of temperature change on input voltage is shown in Fig. 18C, indicating a maximum temperature change of 0.46 °C with an 18 V (p-p) input, which decreases to 0.08 °C with a 10 V (p-p) input.

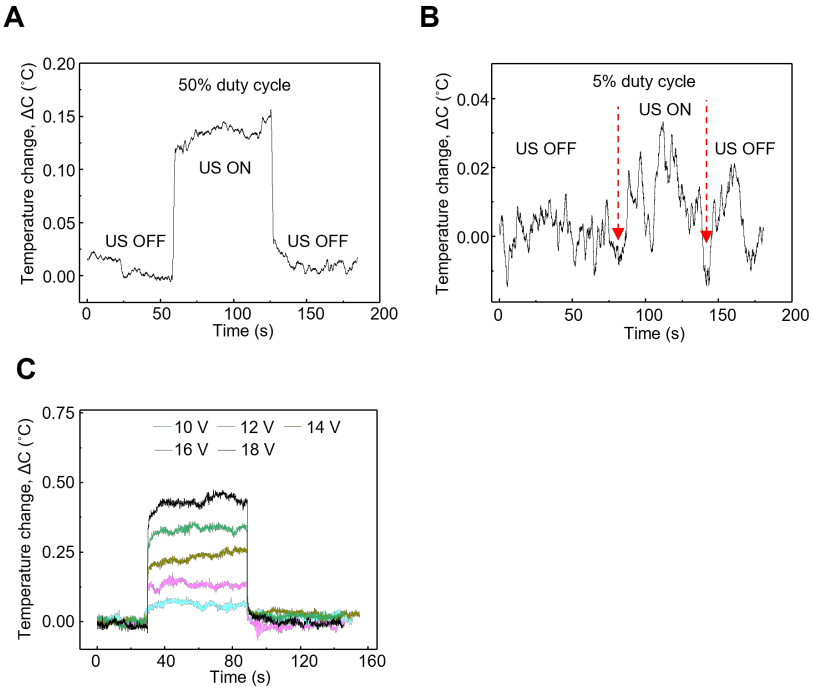

Figure 18: Temperature stability of ImPULS. Change in temperature when (A) 50% duty cycle (B) 5% duty cycle, pulsed signal at 500 kHz is applied. (C) Change in temperature at different input voltages of continuous sinusoidal signal at 500 kHz.

In our ex vivo and in vivo neurostimulation experiments, a maximum of 10 V (p-p) is applied as will be described in later sections. Fig. 2I shows the temperature profile mapping upon application of continuous sinusoidal signal where a maximum temperature change of 0.34 °C occurred, at 15 µm away in the z-direction from the probe center.

4.6 ACCELERATED AGING TEST

To test that ImPULS remains functional over a long period of use within a harsh biological environment, we tested the durability of ImPULS by performing an accelerated aging test in a phosphate-buffered saline (PBS) solution at an elevated temperature of 75 °C for 7 days (Fig 19). Fig. 19 shows microscopic images of ImPULS taken each 24 hours apart, where there is minimal damage visually to the device after 7 days of continuous exposure to PBS at 75 °C. To confirm the device remains fully functional, we measured the displacement of ImPULS before and after 7 days of aging test. As shown in Fig. 19, the displacement of the device degrades only 2.4% in 7 days. To test the durability of ImPULS further, we performed a fatigue test where a continuous sinusoidal signal of 500 kHz at 10 V (p-p) was applied continuously for 7 days and corresponding output displacement was recorded in water medium. As shown in Fig. 19, exposure to 302.4 billion cycles of a sine wave in 7 days results in a 40% lower amplitude of initial displacement, as degradation of the piezoelectric layer after extended electric cycling is a common phenomenon [36], further investigation of fatigue behavior is necessary in future studies.

The accelerated aging test was conducted by inserting test devices and an encapsulated thermistor inside a beaker containing phosphate-buffered saline (PBS) solution. The beaker was placed on top of a hot plate and the temperature was maintained at 75 °C. Because there is a temperature difference between the stage of the hot plate and the PBS inside a beaker, we adjusted the hot plate temperature to 95 °C and used a thermistor to check the inside temperature to remain constant at 75 °C. The beaker was capped with a 3D-printed cap to ensure the PBS did not evaporate during the test time. The PBS solution was replaced with fresh PBS after three days. The displacement of the device was measured before starting the experiment and at the end of the 7th day using a LDV as explained above. Three devices were tested for the accelerated aging test.

4.7 ELECTROMECHANICAL FATIGUE

The device fatigue test was conducted by submerging probes in water and continuously applying a sinusoidal signal (10 V p-p) at their respective resonant frequencies. The probes were kept submerged under water and displacement was measured every day at a fixed time for 7 days. The devices used for this

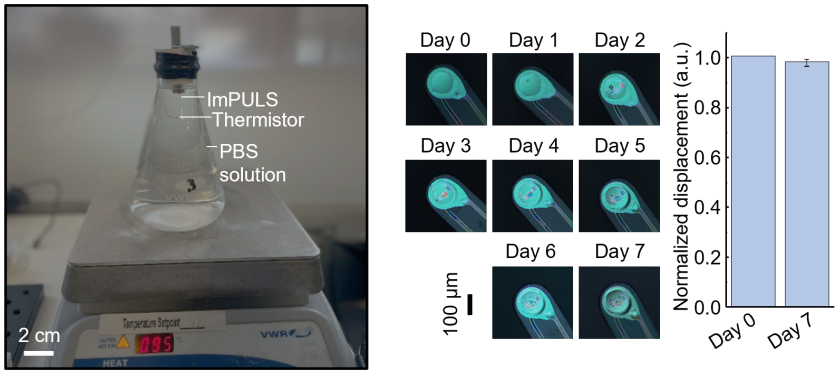

Figure 19: (Left) Aging test setup of ImPULS. Hotplate temperature was adjusted to 95°C to maintain the temperature of PBS solution constant at 75°C which was measured using a thermistor. (Right) Microscopic image of ImPULS taken each 24 h apart during aging test and normalized displacement of ImPULS before start of test and after 7 days.

test had cavities of 105 µm and a resonant frequency of 500 kHz. Therefore, each device was exposed to 302.4 billion cycles of the sinusoidal signal.

4.8 DAMAGE DURING SURGICAL INSERTION

ImPULS was surgically implanted in the deep brain for neurostimulation. To confirm that surgical implantation did not deteriorate its performance, we tested ImPULS performance before and after insertion into brain tissue-mimicking phantom. We prepared 0.6% agar gel to mimic the similar stiffness properties of brain tissue[5][31] and measured the displacement of ImPULS before and after insertion into the gel with a 3-axis stage as shown in Fig. **??**. After insertion, we kept the devices inside the gel for 5 min before removing the device from the gel. As shown in Fig. **??**, the change in displacement is less than 1.5% confirming the device's stability after implantation into the brain tissues.

4.9 EX-VIVO VALIDATION IN BRAIN SLICE

ImPULS was evaluated for its potential to stimulate healthy neurons in a coronal hippocampal slice with two-photon imaging (Fig. 22). Hippocampal neurons expressed the genetically encoded calcium indicator GCaMP7F to report neural

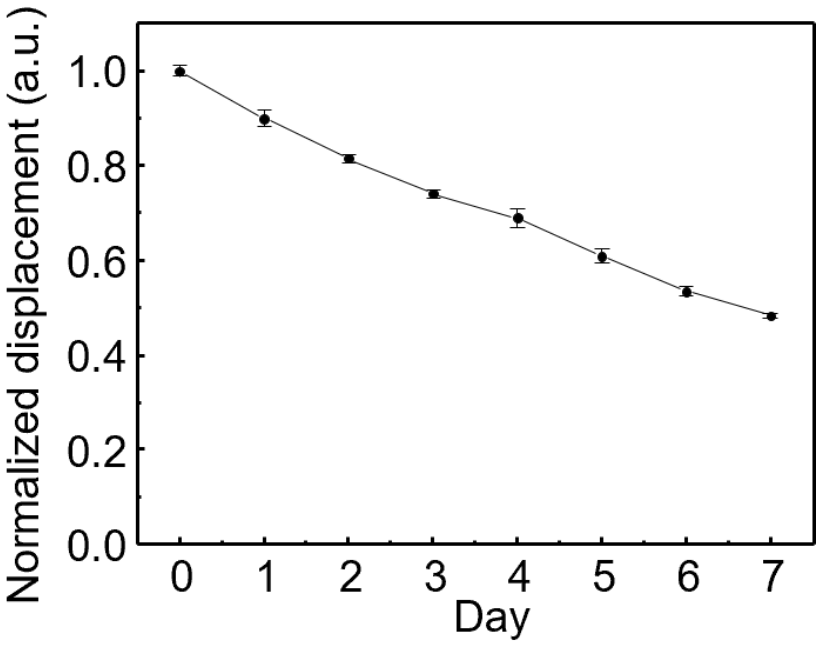

Figure 20: The displacement was measured as an indicator of performance over 7 days with continuous application sinusoidal signal (500 kHz, 10 V (p-p)). The device was submerged in water for 7 days with input signal continuously ON. The measurement was performed 24 h apart for 7 days.

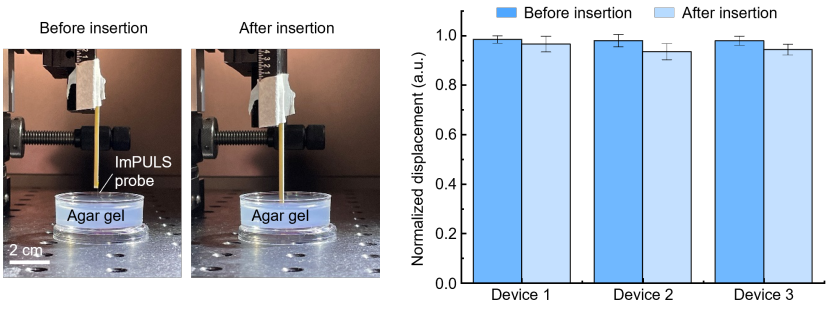

Figure 21: Optical photo of test setup for inserting ImPULS into 0.6% agarose gel and normalized displacement of ImPULS measured before and after insertion into 0.6% agarose gel

activity during ultrasonic stimulation. Neurons in the dentate gyrus were targeted for stimulation (Fig. 22). After a 60 s baseline period, a sinusoidal pulse (500 kHz, 10 V(p-p) with 1.5 kHz pulse repetition frequency (PRF) and

50% duty factor) is used to stimulate neurons for 50 s. After stimulation ends, population activity is captured for another 60 s. Several neurons in our field of view were activated during ultrasound stimulation (Fig. 23). Region of interest 1 (ROI 1) exhibits a 30% change in fluorescence approximately 15 s after stimulation begins and reaches maximum intensity 9 s after the initial rise. The other marked neurons belong to the same local cluster and show smaller changes in activity during stimulation. The delay in neural activation could be due to high amounts of dissolved gasses in the artificial cerebrospinal fluid (aCSF), which may lower cavitation thresholds and cause ultrasound energy from small sources to be absorbed into the medium rather than the tissue [60][25]. In the absence of other stimuli, including the effects on active vasculature [11][20], these results demonstrate that ImPULS can activate local hippocampal neurons.

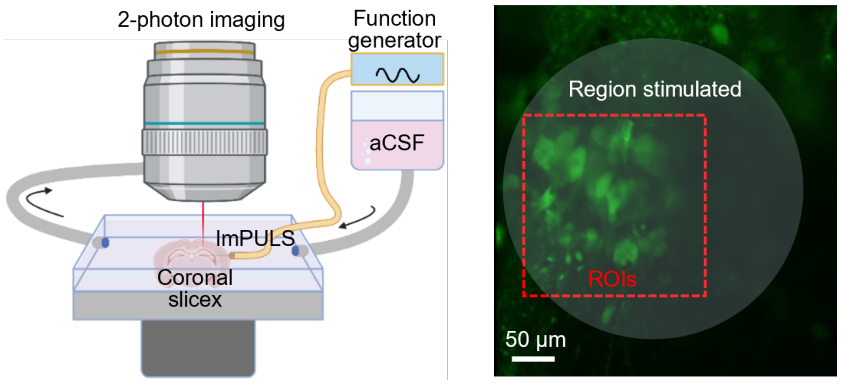

Figure 22: **Two-photon calcium imaging of dentate gyrus in ex-vivo slice model.** (Left) Schematic diagram of the two-photon imaging setup with a coronal hippocampal slice and ImPULS device under magnification. Artificial cerebrospinal fluid (aCSF) is circulated throughout the bath and a function generator connected to leads outside the bath provide the excitation for ultrasonic stimulation. (Right) View of the region of stimulation and neurons targeted (100 µm) above the device.

Acute brain slices were prepared to measure calcium dynamics during ultrasound stimulation ex-vivo. All experiments were conducted in compliance with Boston University Institutional Animal Care and Use Committee (IACUC) approved protocol 201800599. Adult C57BL/6J mice (JAX, strain #000664) of either sex were intracortically injected with an adeno-associated virus for non-specific expression of GCaMP7f (AAV9-syn-jGCaMP7f-WPRE) in the hippocampus at coordinates -2.0 AP, -1.4 ML, -2.0 DV. Acute coronal

slices of the hippocampus were prepared at least 3 weeks following injection. After anesthetization with isoflurane and decapitation, brains were extracted and immersed in 0 °C sucrose-substituted artificial cerebrospinal fluid (in mM): sucrose (185), KCl (2.5), NaH_2PO_4 (1.25), $MgCl_2$ (10), $NaHCO_3$ (25), Glucose (12.5), $CaCl_2$ (0.5). Slices were cut to a thickness of 250 µm (Leica VT 1200, Leica Microsystems). Slices were then incubated at 35°C for 30 min in artificial cerebrospinal fluid (ACSF) consisting of the following (in mM): NaCl (125), $NaHCO_3$ (25), D-glucose (25), KCl (2), $CaCl_2$ (2), NaH_2PO_4 (1.25) and $MgCl_2$ (1). Afterwards, slices were cooled to room temperature (20 °C). After the incubation period, slices were moved to the stage of a two-photon imaging system (Thorlabs) with a mode-locked Titanium:Sapphire laser (Chameleon Ultra II; Coherent) set to a wavelength of 910 nm to excite GCaMP7f using a 20X, NA 1.0 (Olympus) objective lens. Laser scanning was performed using resonant scanners and fluorescence was detected using a photo-multiplier tube (Hamamatsu) equipped with a green filter to record emission from GCaMP7f . The stage of the microscope contained recirculating ACSF perfused with 95% O_2 / 5% CO_2. The temperature of the bath was heated between 35-37°C. A video with 1365 frames and a duration of 170 seconds was captured with a frame rate of 8.02 frames per second.

Fluorescence emission intensities were extracted from the captured video and processed by the CaImAn Python package. Frames in the video are first processed for motion correction, which was negligible due to the fixed nature and minimal drift of the slice. Next, a constrained non-negative matrix factorization (CNMF) algorithm is used for source extraction and deconvolution in order to extract the spatial and temporal components within the frames. Finally, components are automatically evaluated based on the signal-to-noise ratio (SNR), spatial correlation, and neuron shape likelihood (based on a convolutional neural network) of the segmented components. Significant fluorescent traces are manually chosen and the background-normalized change in fluorescence is calculated for each neuron to determine the $\Delta F/F_0$ by percent.

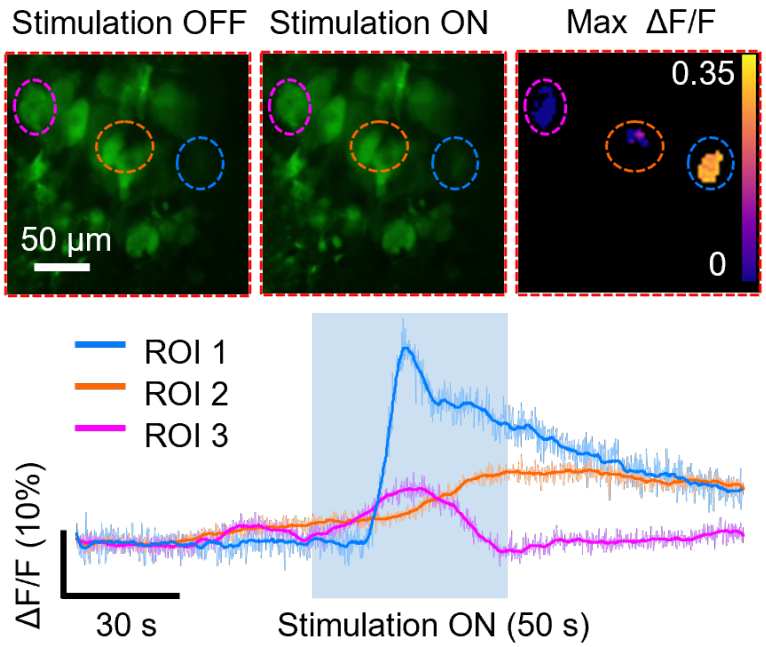

Figure 23: **Two-photon calcium imaging traces.** Averaged frames of the 'Stimulation OFF' period preceding the 'Stimulation ON' period showing three regions of interest (ROI). The normalized maximum fluorescence change for each ROI is depicted as an image mask and the corresponding raw traces for each ROI are shown over the course of the recording session.

5 IN-VIVO DEMONSTRATIONS OF IMPULS

5.1 STIMULATION OF CA1 IN ANESTHETIZED MICE INDUCES CFOS EXPRESSION

We next sought to test the potency of ImPULS to activate cellular ensembles in vivo in mice. To do so, we surgically implanted the ImPULS in the hippocampus–a subcortical brain region that is essential for learning and memory across mammalian species [24] 24. Specifically, we targeted the device to the dorsal CA1 (dCA1) layer of the hippocampal formation to test the efficacy of different stimulation protocols. We quantified the relative levels of cFos in dCA1, which is a widely used marker of recent neuronal activity, to measure the extent of neural activation resulting from different ImPULS stimulations under anesthesia [14]. Compared to a no-stimulation (control) group, we observed an approximately 2-fold increase in cFos expression following stimulation with 500 kHz 10% duty factor, suggesting that this stimulation parameter was sufficient to activate large populations of cells in the dCA1 layer of the mouse hippocampus 25263233.

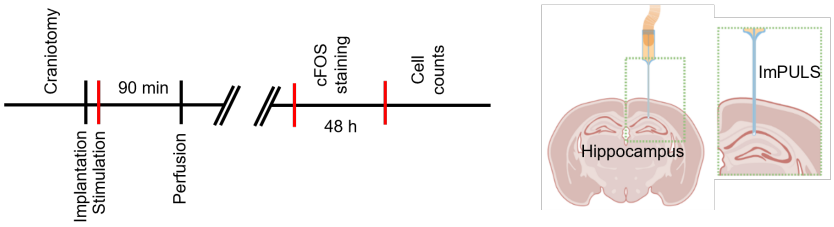

Figure 24: Experimental design and schematic diagram of surgical procedure.

In particular, ultrasound of 500 kHz with 10% duty factor induced the largest increase in cFos expression compared to the continuous signal of 500 kHz. We quantified significant increases in cFos expression along the entirety of dCA1. We were also able to visualize auxiliary cFos expression in CA3 and DG that could be due to backward propagating action potentials, local circuit increases in cFos resulting from ImPULS stimulation spread, and intra-

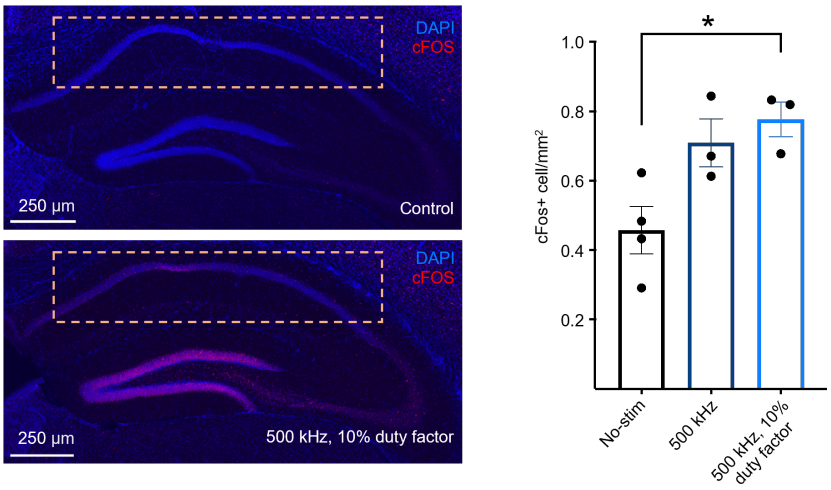

Figure 25: (Left) Representative images of hippocampus across experimental conditions: No-stim (top), and 500 kHz, 10% duty factor for 60s (bottom). Boxed area bounds the dCA1 area used for cell counts. (Right) cFos+ cells in dCA1 normalized by area across experimental conditions (N = 3-4 mice per condition; No-stim vs. 500 kHz: p=0.0506; No-stim vs. 500 kHz, 10% duty factor: p = 0.0184).

hippocampal communication in general[13], which nonetheless underscore the potency of our stimulation parameters. Together, these results demonstrate the applicability of in vivo neuronal stimulation using ImPULS.

5.1.1 Methods & Experimental Preparation

We devised an experimental paradigm to evaluate tissue activation resulting from ultrasound stimulation (US). All experimental protocols were approved by the Institutional Animal Care and Use Committee at Boston University. Mice underwent stereotactic implantation of the ImPULS device into the dCA1 of the hippocampus at the following coordinates: coordinates AP -2.00 mm, ML +1.40 mm, DV -1.50 mm. When these coordinates were reached, 5 min elapsed before stimulation to allow the probe to settle in the surrounding tissue. The ImPULS was positioned to face posteriorly in the anterior-posterior axis so the probe tract could be visualized. The device was secured using dental cement and subjects were allowed to recover before timed perfusions.

All mice were perfused 90-min following ultrasound stimulation to capture peak cFos expression. Mice were first overdosed with isoflurane before

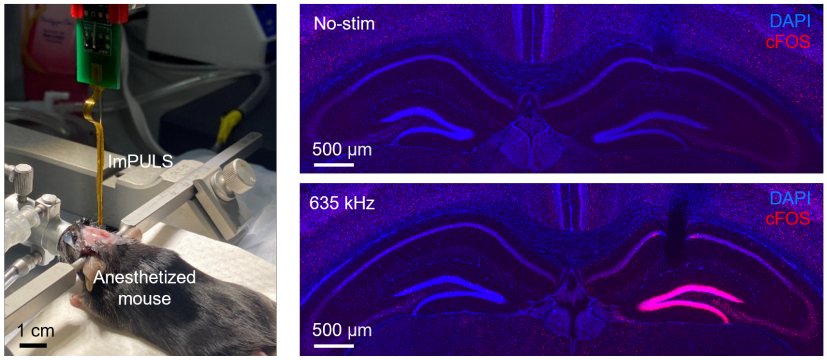

Figure 26: (A) Optical photograph of ImPULS during stereotaxic implantation procedure into the dCA1 hippocampus of an anesthetized mouse. ImPULS was implanted to right hemisphere for stimulation. (B) Representative histology depicting a cross-section of the hippocampus during different experimental conditions: No-stim (Top), 635 kHz for 60s (Bottom). The probe tract can be visualized in the right hippocampus and DAPI+ cells are depicted in blue and cFos+ cells were labeled in red. The left hemisphere was used as negative control for immunohistochemistry.

undergoing transcardial perfusions with 4 °C phosphate buffered saline (PBS) followed by 4% paraformaldehyde (PFA) in PBS. Intact brains were postfixed with the probe still inside for 72 h to facilitate visualization of the probe tract. Tissue sections (50-µm thickness) were then collected using a Leica VT1000 S vibratome equipped with a platinum coated double edged blade (Electron Microscopy Sciences, Cat. #72003-01) and set to a maximal speed of 0.9 mm/s. Sections were chosen based on their proximity to the implantation site - where the probe tract could be directly visualized and those directly anterior and posterior to it. Sections were stained for cFos and then mounted onto micro slices (VWR International, LLC). Vectashield HardSet Mounting Medium with DAPI was applied and slides were coverslipped. All slides were given 12 hours to dry at room temperature before imaging. Slices were imaged utilizing an Akoya Biosciences Vectra Polaris Imaging System at 20x magnification. Images were then aligned to the Allen Brain Reference Atlas to determine the bounds of the dCA1 area and cropped accordingly. Cell counts were calculated for the entire dCA1 layer across the medial-lateral axis of the implanted hippocampus. cFos positive cells were quantified using QuPath, a machine-learning based bioimage analysis pipeline used to classify regions of interest[1]. Histological images were chosen at random to serve as training data in the QuPath program. cFos positive cells were identified and counted by the algorithm with the exper-

imenter blind to treatment and context groups. Counts for cFos positive cells were normalized to the total area of the ROI (counts/mm^2).

5.2 ULTRASOUND STIMULATION OF THE SNC MODULATES NIGROSTRIATAL DOPAMINE RELEASE IN ANESTHETIZED MICE

Next, we tested the utility of ImPULS stimulation for functional modulation of neurotransmission in vivo in mice. Dopaminergic neurons of the SNc innervate the dorsal striatum (DS) to form the canonical nigrostriatal dopamine (DA) pathway, a circuit crucial for movement and reinforcement in the mammalian brain. Furthermore, excitatory stimulation of dopaminergic transmission has therapeutic implications in the treatment of Parkinson's Disease and memory disorders [62][61]. Therefore, we sought to modulate nigrostriatal DA release through ImPULS stimulation of the SNc using an anesthetized preparation (Fig. 27). Specifically, we targeted ImPULS implantation to the anterior SNc with a lateral stimulation direction and performed fiber photometry recordings of extracellular DA release in the DS using a genetically encoded DA sensor, GRAB-DA2m [69]. Further details describing the surgical approach, recording parameters, and data analysis can be found in the supplementary information. Pulsed (PRF 1500 Hz, 50% duty factor) stimulation of the SNc for 5 seconds (514 kHz, 10 V(p-p)) elicited robust, time-locked increases in striatal DA release (Fig. 28). Notably, control stimulation trials, in which we stimulated tissue approximately 200 µm dorsal to the SNc, failed to alter DA2m fluorescence (Fig. 28, top). In contrast, we observed a mean increase in DA2m fluorescence between 2 and 3 Z-scores throughout the duration of ImPULS-mediated SNc stimulation (Fig. 28, bottom). This suggests that ImPULS evokes nigrostriatal DA release in a spatially localized manner. In a second mouse, we observed a mean increase in DA2m fluorescence between 3 and 4 Z-scores throughout ImPULS-mediated SNc stimulation for 1.5 seconds with these same parameters (Fig. 29), indicating that stimulation of shorter durations is sufficient to induce DA release. In a third mouse, however, we observed a mean decrease in DA2m fluorescence between 2 and 3 Z-scores throughout ImPULS-mediated stimulation for 5 seconds with these parameters (Fig. 30). Sections of the SNc were stained for tyrosine hydroxylase (TH), a widely used marker of dopamine-

producing cells, to validate that the ImPULS probe tract contacted dopaminergic neurons in the SNc (Fig. 27).

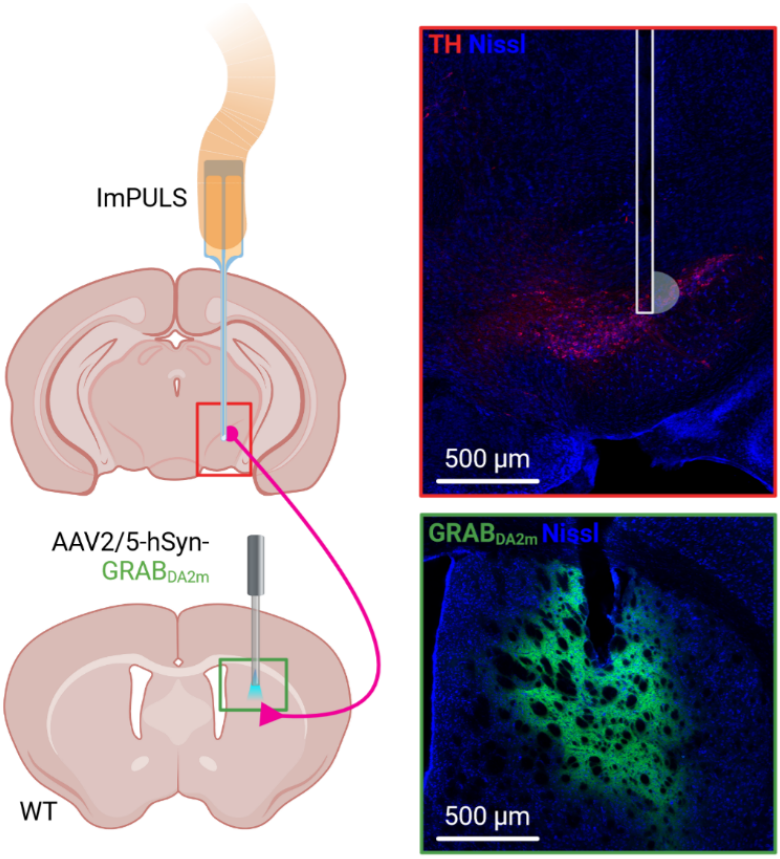

Figure 27: Schematic diagram of the experimental approach to stimulate SNc DA neurons, including post-hoc histological validation of on-target implantation and DA2m sensor expression.

There are two plausible explanations for the inhibition of nigrostriatal DA release. First, ImPULS may elicit both excitatory and inhibitory effects through an unknown underlying mechanism. However, a more likely explanation is due to the limitations of the surgical approach and lack of cell-type specificity for ImPULS stimulation. The substantia nigra pars reticulata (SNr), which is predominantly composed of GABAergic neurons, is situated directly ventral to the SNc and provides monosynaptic inhibitory input to DAergic neurons [59]. Given that the SNc DAergic neurons are angled on the medial-lateral axis and the direction of ImPULS stimulation was lateral, it is feasible that stimulation reached a significant number of SNr inhibitory neurons in this

particular case, effectively silencing DAergic neurons. Furthermore, the tip of the probe tract for this case reached the ventral most portion of the SNc. Together, these data demonstrate that spatially localized deep-brain ultrasound stimulation is capable of modulating neurotransmission in vivo, even through long-range projections.

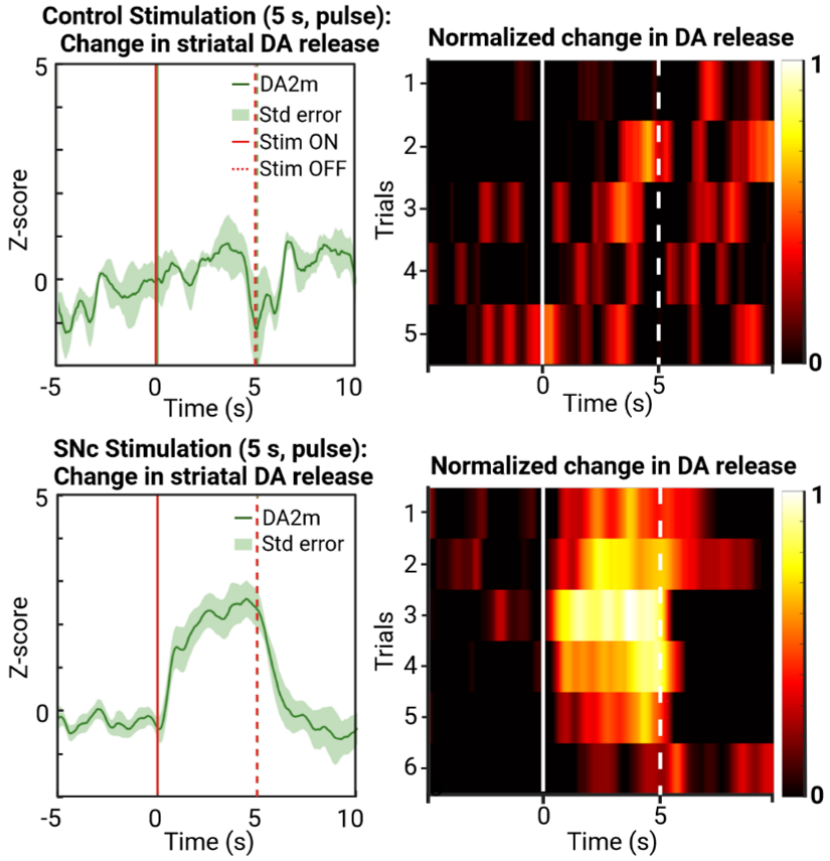

Figure 28: (A) Optical photograph of ImPULS during stereotaxic implantation procedure into the dCA1 hippocampus of an anesthetized mouse. ImPULS was implanted to right hemisphere for stimulation. (B) Representative histology depicting a cross-section of the hippocampus during different experimental conditions: No-stim (Top), 635 kHz for 60s (Bottom). The probe tract can be visualized in the right hippocampus and DAPI+ cells are depicted in blue and cFos+ cells were labeled in red. The left hemisphere was used as negative control for immunohistochemistry.

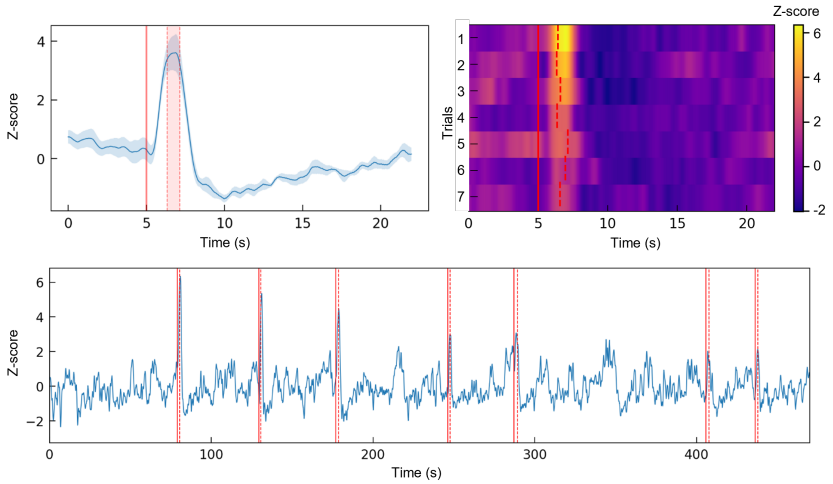

Figure 29: For mouse 2, averaged DA2m fluorescence responses for SNc and heatmap showing relative Z-score of each stimulation trial (top). First solid red line indicates stimulation start time. Shaded region bounded by dotted lines indicates range of stimulation end times. Full recording trace of Z-score DA2m fluorescence during stimulation trial (bottom)

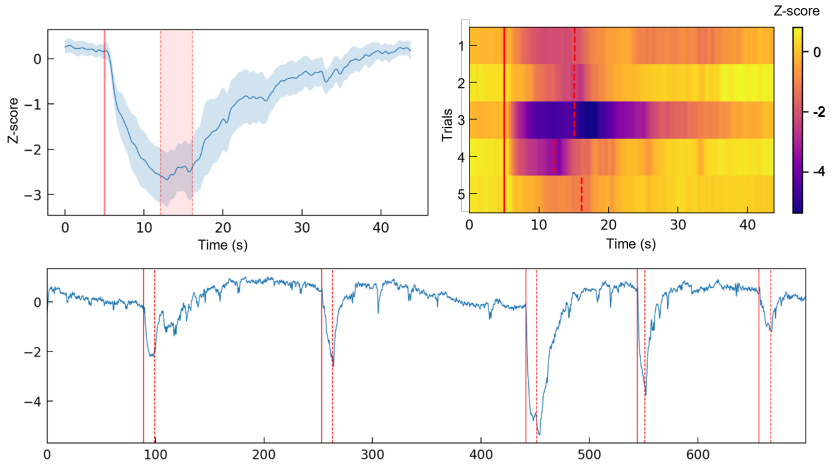

Figure 30: For mouse 3, averaged DA2m fluorescence responses for SNc and heatmap showing relative Z-score of each stimulation trial (top). First solid red line indicates stimulation start time. Shaded region bounded by dotted lines indicates range of stimulation end times. Full recording trace of Z-score DA2m fluorescence during stimulation trial (bottom).

5.2.1 Methods & Experimental Preparation

Adult (P42) female mice received intracranial stereotactic AAV injections under isoflurane anesthesia. AAV expressing hSyn-GRAB-DA2m (AAV2/5, Boston Children's Hospital Viral Core) was injected bilaterally into the dorsal striatum (250 nL/per site, 1x1013 vg/mL titer) at the following coordinates: AP +0.85 mm, ML: +/-1.80 mm, DV from bregma: -3.10 mm, and then implanted with optic fiber cannulas (200-µm core, 0.50 NA) above the injection site at DV -3.00 mm. Three weeks later, the ImPULS probe was slowly lowered into the SNc at the following coordinates: AP -3.10 mm, ML +/-1.00 mm, DV -4.20 to 4.40 mm. Mice were maintained at 1.0% isoflurane anesthesia throughout the recording protocol. Stimulation trials were recorded when the probe reached 200 µm above the SNc (control) and when the probe made contact with the SNc. Pulsed (PRF 1500 Hz, 50% duty factor) stimulation of a set duration in seconds (514 kHz, 10 V) was delivered in each trial using a microcontroller (Teensy 4.0) running a custom script to trigger the output of the function generator and control the pulse repetition frequency, duty factor, trigger signals for the photometry inputs, and stimulation duration. Fiber photometry data were acquired with 410 and 470 nm µLEDs (40 µW power from the tip of connector) at 90 fps (8.50 ms exposure, gain 1.0) using the RWD tricolor fiber photometry system (R820). Using a 60 s time window in the RWD analysis software, DF/F and Z-score data were computed after smoothing (W=15), baseline correction (β=8), and motion correction with the isosbestic signal. Using custom MATLab scripts, mean Z-score fluorescence and standard error of stimulation-triggered responses were calculated and plotted. Heatmaps were generated using a bin size of 50 ms and a normalized colormap (0-1) based on the maximum and minimum Z-score fluorescence.

At the completion of recording, mice were deeply anesthetized and perfused transcardially. Specimens were post-fixed overnight in 4% PFA and then cryoprotected using 30% sucrose solution. Serial coronal sections (80 µm thickness) of the DS and SNc were collected by cryostat sectioning. Tissue sections containing the DS were stained with NeuroTrace Nissl 435/455 (1:500, ThermoFisher, Cat. #N21479) to label cell bodies. Sections containing the SNc were stained for TH and NeuroTrace Nissl. Briefly, sections were incubated with a rabbit anti-TH (1:1500, Millipore, Cat. #AB152) primary antibody, followed by a donkey anti-rabbit Alexa Fluor 647 (1:500, ThermoFisher, Cat. #A-31573) secondary antibody and NeuroTrace Nissl 435/455 (1:500, ThermoFisher, Cat. #N21479) to label neuronal cell bodies. Histological images were acquired using a Zeiss LSM700 confocal microscope.

6 CONCLUDING THOUGHTS

This work presents a micron-sized implantable ultrasound stimulator capable of modulating neuronal activity in deep subcortical regions and nigrostriatal dopamine production across long-range projections. We demonstrate the scalable microfabrication of ImPULS, including the use of biocompatible materials such as the active piezoelectric element (KNN), interconnects, and encapsulation, as well as control over resonance frequency within the range of 0.2-1 MHz through manipulation of cavity size. ImPULS can generate ultrasound pressures of 100 kPa at resonance frequency in pulsed and continuous waves within its stimulation region and evoke modulation of cell activity without causing thermogenic effects on nearby cells. The demonstrated capacity to elicit neuronal excitation in the hippocampus ex vivo, induce activity-dependent gene expression in hippocampal cells of an anesthetized mouse, and modulate dopaminergic neurons in the SNc to elicit precise timing of striatal dopamine release, presents ImPULS as a potent neuromodulatory instrument. Future studies can be spearheaded to gain finer control of stimulation and to evaluate potentially distinct effects of ImPULS-mediated stimulation (i.e. excitation vs inhibition) on different cell types, neural circuits, and regions. By using the targeted stimulation capability of ImPULS together with different acoustic parameters, we believe this implanted ultrasound stimulation device can be developed into a versatile tool for both basic systems neuroscience research and potential therapeutic applications.

A | APPENDIX

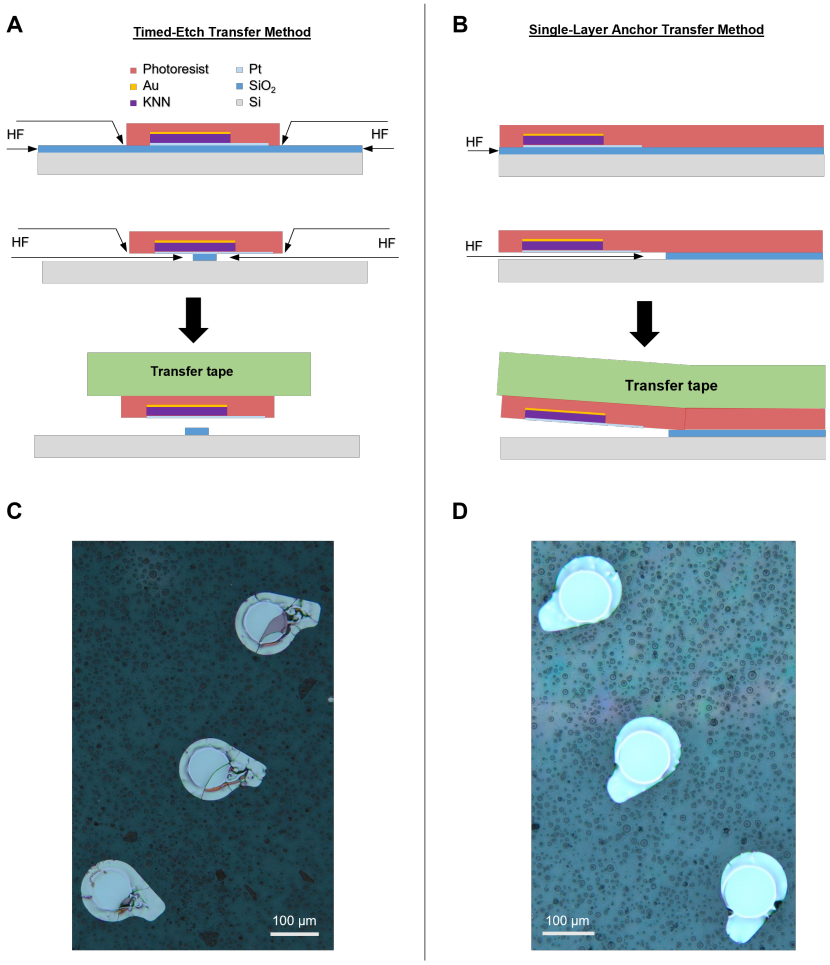

Figure 31: **Comparison of transfer printing using two different types of anchor layer patterning.** (A) Time-etch transfer method (B) Single-layer anchor transfer method (C) Microscopic image of time-etch transferred pattern. This type of transfer creates crack on the bottom Pt electrode. (D) Microscopic image of Single-layer anchor transfer pattern. No crack forms in bottom electrode during transfer. This method is less time sensitive, and therefore improves the yield significantly.

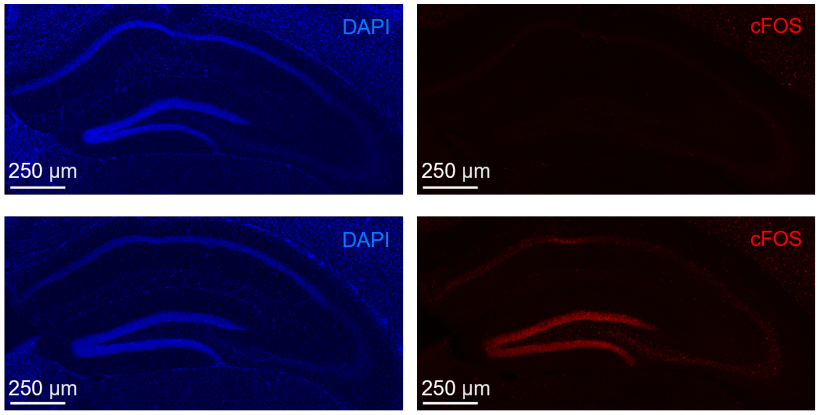

Figure 32: Color-channel separated images by DAPI (left) and cFos (right) of the representative images shown in Fig. 25

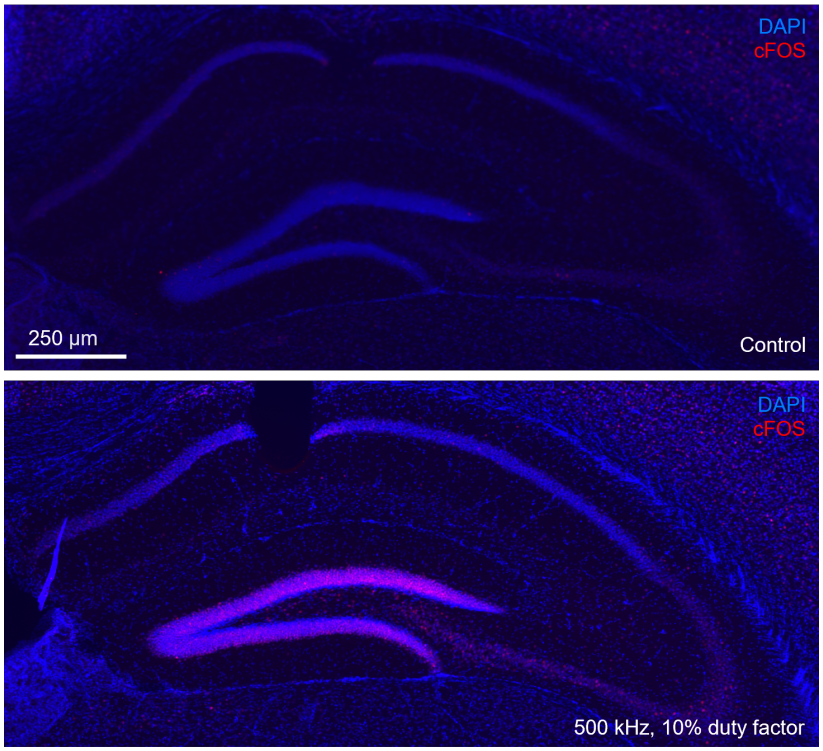

Figure 33: Representative histology of a tissue void depicting the probe tract of ImPULS and the termination of the stimulation location.

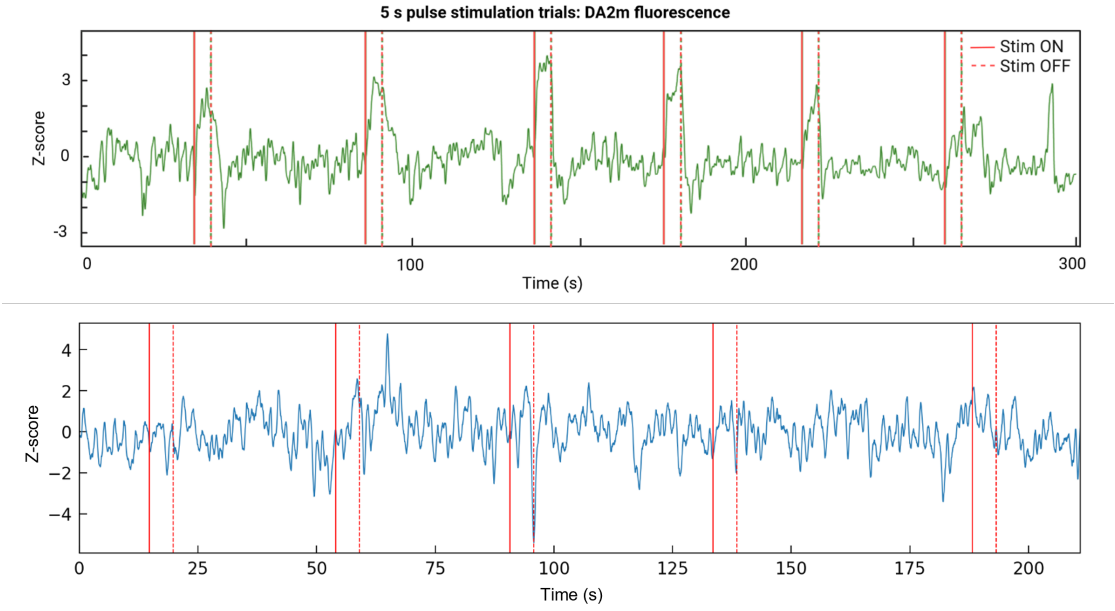

Figure 34: (Top) Full recording trace of Z-score DA2m fluorescence across stimulation trials, with onset and offset of stimulation (5 s,1500 Hz, 50% duty factor) indicated by solid and dashed red lines, respectively. (Bottom) Waveform of stimulation in location approximately 200 µm dorsal to the target stimulation location (control).

BIBLIOGRAPHY

[1] Peter Bankhead, Maurice B. Loughrey, José A. Fernández, Yvonne Dombrowski, Darragh G. McArt, Philip D. Dunne, Stephen McQuaid, Ronan T. Gray, Liam J. Murray, Helen G. Coleman, Jacqueline A. James, Manuel Salto-Tellez, and Peter W. Hamilton. Qupath: Open source software for digital pathology image analysis. *Scientific Reports*, 7(1):16878, Dec 2017.

[2] G. Bertotti, Isaak Mayergoyz, and Dragan Damjanovic. Hysteresis in piezoelectric and ferroelectric materials. 01 2006.

[3] Ritchie Chen, Gabriela Romero, Michael G. Christiansen, Alan Mohr, and Polina Anikeeva. Wireless magnetothermal deep brain stimulation. *Science*, 347(6229):1477–1480, 2015.

[4] Wei Chen, Zunxiong Yu, Jinshan Pang, Peng Yu, Guoxin Tan, and Chengyun Ning. Fabrication of biocompatible potassium sodium niobate piezoelectric ceramic as an electroactive implant. *Materials*, 10(4), 2017.

[5] Zhi-Jian Chen, George T. Gillies, William C. Broaddus, Sujit S. Prabhu, Helen Fillmore, Ryan M. Mitchell, Frank D. Corwin, and Panos P. Fatouros. A realistic brain tissue phantom for intraparenchymal infusion studies. *Journal of Neurosurgery*, 101(2):314 – 322, 2004.

[6] Canan Dagdeviren, Khalil B. Ramadi, Pauline Joe, Kevin Spencer, Helen N. Schwerdt, Hideki Shimazu, Sebastien Delcasso, Ken ichi Amemori, Carlos Nunez-Lopez, Ann M. Graybiel, Michael J. Cima, and Robert Langer. Miniaturized neural system for chronic, local intracerebral drug delivery. *Science Translational Medicine*, 10(425):eaan2742, 2018.

[7] Canan Dagdeviren, Yan Shi, Pauline Joe, Roozbeh Ghaffari, Guive Balooch, Karan Usgaonkar, Onur Gur, Phat L. Tran, Jessi R. Crosby, Marcin Meyer, Yewang Su, R. Chad Webb, Andrew S. Tedesco, Marvin J. Slepian, Yonggang Huang, and John A. Rogers. Conformal piezoelectric systems for clinical and experimental characterization of soft tissue biomechanics. *Nature Materials*, 14(7):728–736, Jul 2015.

[8] Diane Dalecki. Mechanical bioeffects of ultrasound. *Annual Review of Biomedical Engineering*, 6(1):229–248, 2004. PMID: 15255769.

[9] David P. Darrow. Focused ultrasound for neuromodulation. *Neurotherapeutics*, 16(1):88–99, Jan 2019.

[10] David P. Darrow, Parker O'Brien, Thomas J. Richner, Theoden I. Netoff, and Emad S. Ebbini. Reversible neuroinhibition by focused ultrasound is mediated by a thermal mechanism. *Brain Stimulation*, 12(6):1439–1447, 2019.

[11] Catherine M. Davis, Azzdine Y. Ammi, Nabil J. Alkayed, and Sanjiv Kaul. Ultrasound stimulates formation and release of vasoactive compounds in brain endothelial cells. *American Journal of Physiology-Heart and Circulatory Physiology*, 309(4):H583–H591, 2015. PMID: 26092990.

[12] Archy De Berker, Marom Bikson, and Sven Bestmann. Predicting the behavioral impact of transcranial direct current stimulation: issues and limitations. *Frontiers in Human Neuroscience*, 7, 2013.

[13] Michael S. Fanselow and Hong-Wei Dong. Are the dorsal and ventral hippocampus functionally distinct structures? *Neuron*, 65(1):7–19, 2010.

[14] Steven W. Flavell and Michael E. Greenberg. Signaling mechanisms linking neuronal activity to gene expression and plasticity of the nervous system. *Annual Review of Neuroscience*, 31(1):563–590, 2008. PMID: 18558867.

[15] Davide Folloni. Ultrasound neuromodulation of the deep brain. *Science*, 377(6606):589–589, 2022.

[16] Adriana Galvan, William R. Stauffer, Leah Acker, Yasmine El-Shamayleh, Ken ichi Inoue, Shay Ohayon, and Michael C. Schmid. Nonhuman primate optogenetics: Recent advances and future directions. *Journal of Neuroscience*, 37(45):10894–10903, 2017.

[17] Nikolai Helth Gaukås, Quy-Susan Huynh, Anishchal A. Pratap, Mari-Ann Einarsrud, Tor Grande, R. M. Damian Holsinger, and Julia Glaum. In vitro biocompatibility of piezoelectric ko.5nao.5nbo3 thin films on platinized silicon substrates. *ACS Applied Bio Materials*, 3(12):8714–8721, Dec 2020.

[18] Hongsun Guo, Mark Hamilton, Sarah J. Offutt, Cory D. Gloeckner, Tianqi Li, Yohan Kim, Wynn Legon, Jamu K. Alford, and Hubert H. Lim. Ultrasound produces extensive brain activation via a cochlear pathway. *Neuron*, 98(5):1020–1030.e4, 2018.

[19] Hongsun Guo, Sarah J. Offutt, Mark Hamilton II, Yohan Kim, Cory D. Gloeckner, Daniel P. Zachs, Jamu K. Alford, and Hubert H. Lim. Ultrasound

does not activate but can inhibit in vivo mammalian nerves across a wide range of parameters. *Scientific Reports*, 12(1):2182, Feb 2022.

[20] Jiecheng Guo, Wai Leung Ambrose Lo, Huijing Hu, Li Yan, and Le Li. Transcranial ultrasound stimulation applied in ischemic stroke rehabilitation: A review. *Frontiers in Neuroscience*, 16, 2022.

[21] Stuart Hameroff, Michael Trakas, Chris Duffield, Emil Annabi, M. Bagambhrini Gerace, Patrick Boyle, Anthony Lucas, Quinlan Amos, Annemarie Buadu, and John J. Badal. Transcranial ultrasound (tus) effects on mental states: A pilot study. *Brain Stimulation*, 6(3):409–415, 2013.

[22] Thomas Heimburg and Andrew D. Jackson. On soliton propagation in biomembranes and nerves. *Proceedings of the National Academy of Sciences*, 102(28):9790–9795, 2005.

[23] Stuart Ibsen, Ada Tong, Carolyn Schutt, Sadik Esener, and Sreekanth H. Chalasani. Sonogenetics is a non-invasive approach to activating neurons in caenorhabditis elegans. *Nature Communications*, 6(1):8264, Sep 2015.

[24] Sheena A. Josselyn and Susumu Tonegawa. Memory engrams: Recalling the past and imagining the future. *Science*, 367(6473):eaaw4325, 2020.

[25] Hermes A. S. Kamimura, Allegra Conti, Nicola Toschi, and Elisa E. Konofagou. Ultrasound neuromodulation: Mechanisms and the potential of multimodal stimulation for neuronal function assessment. *Frontiers in Physics*, 8, 2020.

[26] Maria Kekic, Elena Boysen, Iain C. Campbell, and Ulrike Schmidt. A systematic review of the clinical efficacy of transcranial direct current stimulation (tdcs) in psychiatric disorders. *Journal of Psychiatric Research*, 74:70–86, 2016.

[27] Randy L. King, Julian R. Brown, William T. Newsome, and Kim Butts Pauly. Effective parameters for ultrasound-induced in vivo neurostimulation. *Ultrasound in Medicine & Biology*, 39(2):312–331, 2013.

[28] Masahito Kobayashi and Alvaro Pascual-Leone. Transcranial magnetic stimulation in neurology. *The Lancet Neurology*, 2(3):145–156, 2003.

[29] Marija Kosec, Barbara Malič, Andreja Benčan, and Tadej Rojac. *KNN-Based Piezoelectric Ceramics*, pages 81–102. Springer US, Boston, MA, 2008.

[30] Takashi D. Y. Kozai, Andrea S. Jaquins-Gerstl, Alberto L. Vazquez, Adrian C. Michael, and X. Tracy Cui. Brain tissue responses to neural implants impact signal sensitivity and intervention strategies. *ACS Chemical Neuroscience*, 6(1):48–67, Jan 2015.

[31] Takashi D. Yoshida Kozai and Daryl R. Kipke. Insertion shuttle with carboxyl terminated self-assembled monolayer coatings for implanting flexible polymer neural probes in the brain. *Journal of Neuroscience Methods*, 184(2):199–205, 2009.

[32] Joachim K. Krauss, Nir Lipsman, Tipu Aziz, Alexandre Boutet, Peter Brown, Jin Woo Chang, Benjamin Davidson, Warren M. Grill, Marwan I. Hariz, Andreas Horn, Michael Schulder, Antonios Mammis, Peter A. Tass, Jens Volkmann, and Andres M. Lozano. Technology of deep brain stimulation: current status and future directions. *Nature Reviews Neurology*, 17(2):75–87, Feb 2021.

[33] Jan Kubanek, Jingyi Shi, Jon Marsh, Di Chen, Cheri Deng, and Jianmin Cui. Ultrasound modulates ion channel currents. *Scientific Reports*, 6(1):24170, Apr 2016.

[34] Jungpyo Lee, Kyungmin Ko, Hyogeun Shin, Soo-Jin Oh, C. Justin Lee, Namsun Chou, Nakwon Choi, Min Tack Oh, Byung Chul Lee, Seong Chan Jun, and Il-Joo Cho. A mems ultrasound stimulation system for modulation of neural circuits with high spatial resolution in vitro. *Microsystems & Nanoengineering*, 5(1):28, Jul 2019.

[35] Keng Siang Lee, Benjamin Clennell, Tom G. J. Steward, Andriana Gialeli, Oscar Cordero-Llana, and Daniel J. Whitcomb. Focused ultrasound stimulation as a neuromodulatory tool for parkinsonrsquo;s disease: A scoping review. *Brain Sciences*, 12(2), 2022.

[36] Ruichen Li, Yushun Zeng, Xi-xi Sun, Chongyang Li, Runze Li, Ting Zheng, Laiming Jiang, and Jiagang Wu. Multidimensional synergy-induced high piezoelectricity and reliability knn piezoceramics for high-frequency ultrasonic transducers. *Science China Materials*, 66(2):686–695, Feb 2023.

[37] Xin Li, Huifang Yang, Jiaqing Yan, Xingran Wang, Xiaoli Li, and Yi Yuan. Low-intensity pulsed ultrasound stimulation modulates the nonlinear dynamics of local field potentials in temporal lobe epilepsy. *Frontiers in Neuroscience*, 13, 2019.

[38] Y. Liang, B. E. Eovino, and L. Lin. Pinned boundary piezoelectric micromachined ultrasonic transducers. In *2019 IEEE 32nd International Conference*

on Micro Electro Mechanical Systems (MEMS), 2019 IEEE 32nd International Conference on Micro Electro Mechanical Systems (MEMS), pages 791–794, 2019.

[39] Wei-Hao Liao, Ming-Yen Hsiao, Yi Kung, Hao-Li Liu, Jean-Christophe Béra, Claude Inserra, and Wen-Shiang Chen. Trpv4 promotes acoustic wave-mediated bbb opening via ca2+/pkc- pathway. *Journal of Advanced Research*, 26:15–28, 2020.

[40] Wei-Ting Lin, Ran-Chou Chen, Wen-Wei Lu, Shing-Hwa Liu, and Feng-Yi Yang. Protective effects of low-intensity pulsed ultrasound on aluminum-induced cerebral damage in alzheimer's disease rat model. *Scientific Reports*, 5(1):9671, Apr 2015.

[41] Nir Lipsman, Ying Meng, Allison J. Bethune, Yuexi Huang, Benjamin Lam, Mario Masellis, Nathan Herrmann, Chinthaka Heyn, Isabelle Aubert, Alexandre Boutet, Gwenn S. Smith, Kullervo Hynynen, and Sandra E. Black. Blood–brain barrier opening in alzheimer's disease using mr-guided focused ultrasound. *Nature Communications*, 9(1):2336, Jul 2018.

[42] Thomas J. Manuel, Jiro Kusunose, Xiaoyan Zhan, Xiaohui Lv, Ellison Kang, Aaron Yang, Zixiu Xiang, and Charles F. Caskey. Ultrasound neuromodulation depends on pulse repetition frequency and can modulate inhibitory effects of ttx. *Scientific Reports*, 10(1):15347, Sep 2020.

[43] Cameron C. McIntyre and Warren M. Grill. Finite element analysis of the current-density and electric field generated by metal microelectrodes. *Annals of Biomedical Engineering*, 29(3):227–235, Mar 2001.

[44] Cameron C. McIntyre, Susumu Mori, David L. Sherman, Nitish V. Thakor, and Jerrold L. Vitek. Electric field and stimulating influence generated by deep brain stimulation of the subthalamic nucleus. *Clinical Neurophysiology*, 115(3):589–595, 2004.

[45] Cameron C. McIntyre, Susumu Mori, David L. Sherman, Nitish V. Thakor, and Jerrold L. Vitek. Electric field and stimulating influence generated by deep brain stimulation of the subthalamic nucleus. *Clinical Neurophysiology*, 115(3):589–595, 2004.

[46] Michael D. Menz, Ömer Oralkan, Pierre T. Khuri-Yakub, and Stephen A. Baccus. Precise neural stimulation in the retina using focused ultrasound. *Journal of Neuroscience*, 33(10):4550–4560, 2013.

[47] Svjetlana Miocinovic, Suvarchala Somayajula, Shilpa Chitnis, and Jerrold L. Vitek. History, Applications, and Mechanisms of Deep Brain Stimulation. *JAMA Neurology*, 70(2):163–171, 02 2013.

[48] Paul Morris, Andrew Hurrell, Adam Shaw, Edward Zhang, and Paul Beard. A Fabry–Pérot fiber-optic ultrasonic hydrophone for the simultaneous measurement of temperature and acoustic pressure. *The Journal of the Acoustical Society of America*, 125(6):3611–3622, 06 2009.

[49] Nikita Obidin, Farita Tasnim, and Canan Dagdeviren. The future of neuroimplantable devices: A materials science and regulatory perspective. *Advanced Materials*, 32(15):1901482, 2020.

[50] Soo-Jin Oh, Jung Moo Lee, Hyun-Bum Kim, Jungpyo Lee, Sungmin Han, Jin Young Bae, Gyu-Sang Hong, Wuhyun Koh, Jea Kwon, Eun-Sang Hwang, Dong Ho Woo, Inchan Youn, Il-Joo Cho, Yong Chul Bae, Sungon Lee, Jae Wan Shim, Ji-Ho Park, and C. Justin Lee. Ultrasonic neuromodulation via astrocytic trpa1. *Current Biology*, 29(20):3386–3401.e8, 2019.

[51] Alexander G. Petrov. Electricity and mechanics of biomembrane systems: Flexoelectricity in living membranes. *Analytica Chimica Acta*, 568(1):70–83, 2006. Molecular Electronics and Analytical Chemistry.

[52] Gianmarco Pinton, Jean-Francois Aubry, Emmanuel Bossy, Marie Muller, Mathieu Pernot, and Mickael Tanter. Attenuation, scattering, and absorption of ultrasound in the skull bone. *Medical Physics*, 39(1):299–307, 2012.

[53] Rafael Polanía, Michael A. Nitsche, and Christian C. Ruff. Studying and modifying brain function with non-invasive brain stimulation. *Nature Neuroscience*, 21(2):174–187, Feb 2018.

[54] Flavius Pop, Bernard Herrera, and Matteo Rinaldi. Lithium niobate piezoelectric micromachined ultrasonic transducers for high data-rate intrabody communication. *Nature Communications*, 13(1):1782, Apr 2022.

[55] Yongqiang Qiu, James V. Gigliotti, Margeaux Wallace, Flavio Griggio, Christine E. M. Demore, Sandy Cochran, and Susan Trolier-McKinstry. Piezoelectric micromachined ultrasound transducer (pmut) arrays for integrated sensing, actuation and imaging. *Sensors*, 15(4):8020–8041, 2015.

[56] Zhihai Qiu, Jinghui Guo, Shashwati Kala, Jiejun Zhu, Quanxiang Xian, Weibao Qiu, Guofeng Li, Ting Zhu, Long Meng, Rui Zhang, Hsiao Chang Chan, Hairong Zheng, and Lei Sun. The mechanosensitive ion channel

piezo1 significantly mediates in vitro ultrasonic stimulation of neurons. *iScience*, 21:448–457, 2019.

[57] Khalil B. Ramadi, Canan Dagdeviren, Kevin C. Spencer, Pauline Joe, Max Cotler, Erin Rousseau, Carlos Nunez-Lopez, Ann M. Graybiel, Robert Langer, and Michael J. Cima. Focal, remote-controlled, chronic chemical modulation of brain microstructures. *Proceedings of the National Academy of Sciences*, 115(28):7254–7259, 2018.

[58] Michael C. Ridding and John C. Rothwell. Is there a future for therapeutic use of transcranial magnetic stimulation? *Nature Reviews Neuroscience*, 8(7):559–567, Jul 2007.

[59] Giorgio Rizzi and Kelly R. Tan. Synergistic nigral output pathways shape movement. *Cell Reports*, 27(7):2184–2198.e4, 2019.

[60] Joost Rooze, Evgeny V. Rebrov, Jaap C. Schouten, and Jos T.F. Keurentjes. Dissolved gas and ultrasonic cavitation – a review. *Ultrasonics Sonochemistry*, 20(1):1–11, 2013.

[61] Aryeh Routtenberg and Nancy Holzman. Memory disruption by electrical stimulation of substantia nigra, pars compacta. *Science*, 181(4094):83–86, 1973.

[62] Siddhartha Sahai, Emaan T. Effendi, Emily C. Mahoney, Heidi R. Tucker, Benjamin J. Moolick, Gianna Mamone, Saisree Mikkilineni, Megan Gupta, Alycia Nicholson, Fu Yee Chua, Kainat Akhtar, Zall Hirschstein, Eric S. Molho, Julie G. Pilitsis, and Damian S. Shin. Effects of subthalamic nucleus deep brain stimulation on neuronal spiking activity in the substantia nigra pars compacta in a rat model of parkinson's disease. *Neuroscience Letters*, 739:135443, 2020.

[63] Joseph W. Salatino, Kip A. Ludwig, Takashi D. Y. Kozai, and Erin K. Purcell. Glial responses to implanted electrodes in the brain. *Nature Biomedical Engineering*, 1(11):862–877, Nov 2017.

[64] Tomokazu Sato, Mikhail G. Shapiro, and Doris Y. Tsao. Ultrasonic neuromodulation causes widespread cortical activation via an indirect auditory mechanism. *Neuron*, 98(5):1031–1041.e5, 2018.

[65] Yi Shen, Robert E. Campbell, Daniel C. Côté, and Marie-Eve Paquet. Challenges for therapeutic applications of opsin-based optogenetic tools in humans. *Frontiers in Neural Circuits*, 14, 2020.

[66] Linli Shi, Ying Jiang, Fernando R. Fernandez, Guo Chen, Lu Lan, Heng-Ye Man, John A. White, Ji-Xin Cheng, and Chen Yang. Non-genetic photoacoustic stimulation of single neurons by a tapered fiber optoacoustic emitter. *Light: Science & Applications*, 10(1):143, Jul 2021.

[67] Kenji Shibata, Kazutoshi Watanabe, Toshiaki Kuroda, and Takenori Osada. KNN lead-free piezoelectric films grown by sputtering. *Applied Physics Letters*, 121(9), 08 2022. 092901.

[68] Changhe Sun, Qiongfeng Shi, Mahmut Sami Yazici, Takeshi Kobayashi, Yufei Liu, and Chengkuo Lee. Investigation of broadband characteristics of multi-frequency piezoelectric micromachined ultrasonic transducer (mf-pmut). *IEEE Sensors Journal*, 19(3):860–867, 2019.

[69] Fangmiao Sun, Jianzhi Zeng, Miao Jing, Jingheng Zhou, Jiesi Feng, Scott F. Owen, Yichen Luo, Funing Li, Huan Wang, Takashi Yamaguchi, Zihao Yong, Yijing Gao, Wanling Peng, Lizhao Wang, Siyu Zhang, Jiulin Du, Dayu Lin, Min Xu, Anatol C. Kreitzer, Guohong Cui, and Yulong Li. A genetically encoded fluorescent sensor enables rapid and specific detection of dopamine in flies, fish, and mice. *Cell*, 174(2):481–496.e19, 2018.

[70] Onat Tokay and Murat Yazıcı. A review of potassium sodium niobate and bismuth sodium titanate based lead free piezoceramics. *Materials Today Communications*, 31:103358, 2022.

[71] William J Tyler, Shane W Lani, and Grace M Hwang. Ultrasonic modulation of neural circuit activity. *Current Opinion in Neurobiology*, 50:222–231, 2018. Neurotechnologies.

[72] William J. Tyler, Yusuf Tufail, Michael Finsterwald, Monica L. Tauchmann, Emily J. Olson, and Cassondra Majestic. Remote excitation of neuronal circuits using low-intensity, low-frequency ultrasound. *PLOS ONE*, 3(10):1–11, 10 2008.

[73] Patrick Peiyong Ye, Julian R. Brown, and Kim Butts Pauly. Frequency dependence of ultrasound neurostimulation in the mouse brain. *Ultrasound in Medicine Biology*, 42(7):1512–1530, 2016.

[74] Patrick Peiyong Ye, Julian R. Brown, and Kim Butts Pauly. Frequency dependence of ultrasound neurostimulation in the mouse brain. *Ultrasound in Medicine and Biology*, 42(7):1512–1530, Jul 2016.

[75] Sangjin Yoo, David R. Mittelstein, Robert C. Hurt, Jerome Lacroix, and Mikhail G. Shapiro. Focused ultrasound excites cortical neurons via

mechanosensitive calcium accumulation and ion channel amplification. *Nature Communications*, 13(1):493, Jan 2022.